Complex critical points in Lorentzian spinfoam quantum gravity: Four-simplex amplitude and effective dynamics on a double-Δ_3 complex

Muxin Han,[1,2,*] Hongguang Liu,[2,†] and Dongxue Qu[3,1,‡]

[1]*Department of Physics, Florida Atlantic University, 777 Glades Road, Boca Raton, Florida 33431-0991, USA*

[2]*Department Physik, Institut für Quantengravitation, Theoretische Physik III, Friedrich-Alexander Universität Erlangen-Nürnberg, Staudtstraße 7/B2, 91058 Erlangen, Germany*

[3]*Perimeter Institute for Theoretical Physics, 31 Caroline Street North, Waterloo, Ontario N2L 2Y5, Canada*

(Received 9 February 2023; accepted 24 May 2023; published 20 July 2023)

The complex critical points are analyzed in the four-dimensional Lorentzian Engle-Pereira-Rovelli-Livine spinfoam model in the large-j regime. For the four-simplex amplitude, taking into account the complex critical point generalizes the large-j asymptotics to the situation with non-Regge boundary data and relates to the twisted geometry. For generic simplicial complexes, we present a general procedure to derive the effective theory of Regge geometries from the spinfoam amplitude in the large-j regime by using the complex critical points. The effective theory is analyzed in detail for the spinfoam amplitude on the double-Δ_3 simplicial complex. We numerically compute the effective action and the solution of the effective equation of motion on the double-Δ_3 complex. The effective theory reproduces the classical Regge gravity when the Barbero-Immirzi parameter γ is small.

DOI: 10.1103/PhysRevD.108.026010

I. INTRODUCTION

The perturbative expansion is widely used in quantum theory to make approximate predictions order by order in certain parameter. The method of perturbative expansion is well-connected to the path integral formulation, whose stationary-phase approximation results in the semiclassical expansion in $\hbar$. By the stationary phase approximation, the path integral is approximately computed by the dominant contribution from the critical point and neighborhood. The critical point is the solution of the equation of motion, which is obtained from variating the action in the path integral. Given a path integral in terms of real variables, traditionally, the semiclassical expansion only takes into account critical points inside the real integration cycle. However, the recent progress in many research areas demonstrates that the complex critical point generically away from the real integration cycle plays a crucial role in the semiclassical expansion of the path integral (see e.g., [1–6]). The complex critical point is the critical point of the analytically continued path integral, where the integrand is analytically extended to the complexification of the real integration cycle.

The method of stationary phase approximation has been applied extensively to the spinfoam amplitude in loop quantum gravity (LQG) (see e.g., [7–11]). The importance of the complex critical point has been demonstrated in the recent progress in the semiclassical analysis of spinfoam amplitude [12–14]. A key result is that the semiclassical curved spacetime geometry can only emerge from the complex critical point of the spinfoam amplitude. Taking into account that the complex critical point provides the resolution to the long-standing "flatness problem," i.e., the problem of discovering only the flat spacetime geometry in the spinfoam amplitude. This problem turns out to be the confusion from ignoring the complex critical point.

The present work continues from the earlier work [12] and further study the complex critical points and their implications in spinfoam amplitude. The discussion in this work focuses on the four-dimensional Lorentzian Engle-Pereira-Rovelli-Livine (EPRL) spinfoam model. Our results demonstrate the impact of the complex critical points mainly from two perspectives:

(i) At the level of one four-simplex amplitude, taking into account the complex critical point generalizes the large-j asymptotics by Barrett *et al.* [8] to the case of non-Regge boundary data. The geometry of the non-Regge boundary data gives the boundary tetrahedra that are glued only with area-matching but without shape-matching, in contrast to the Regge

*hanm@fau.edu
†hongguang.liu@gravity.fau.de
‡dqu@perimeterinstitute.ca

boundary data that requires the shape-matching condition (as well as the orientation matching condition) and determines the Regge boundary geometry. The generalized four-simplex amplitude asymptotic behavior depends analytically on the boundary data. This analytic dependence is not manifest in the original asymptotic formula in [8]. The computation of the generalized asymptotic behavior relies on the numerical method. The discussion in Sec. IV provides the general algorithm of computing the complex critical point of the amplitude, and demonstrates the numerical results of the asymptotics for a one-parameter family of non-Regge boundary data.

(ii) Based on the application of complex critical points, we develop a formalism to derive the effective theory of Regge geometry from the large-j spinfoam amplitude. As the result, given a simplicial complex $\mathcal{K}$ with M internal segments, the spinfoam amplitude $A(\mathcal{K})$ with Regge boundary data reduces to the integral over the internal line-segment lengths l_I, $I = 1, \ldots, M$,

$$A(\mathcal{K}) \sim \int \prod_{I=1}^{M} \mathrm{d}\mu(l_I) e^{\lambda \mathcal{S}(\vec{l})} [1 + O(1/\lambda)], \qquad \lambda \gg 1, \tag{1.1}$$

within the neighborhood of the integration domain of $A(\mathcal{K})$. λ is the scaling parameter of spins j_f. $e^{\lambda \mathcal{S}(\vec{l})}$ with the effective action $\mathcal{S}(\vec{l})$ comes from evaluating the analytically continued integrand of $A(\mathcal{K})$ at the complex critical point, which depend analytically on l_I. The integral in (1.1) reduced from $A(\mathcal{K})$ is over the Regge geometries with the fixed boundary condition. The equation of motion $\partial_{l_I} \mathcal{S}(\vec{l}) = 0$ gives the effective dynamics of Regge geometry implied by the spinfoam amplitude. The formalism of deriving the effective theory is discussed in Sec. III. In Secs. VI and VII, we apply the formalism to the double-Δ_3 simplicial complex, which contains only a single internal segment, i.e., $M = 1$. The complex critical points and the effective action $\mathcal{S}(\vec{l})$ are computed numerically following the general algorithm. The spinfoam amplitude depends on the Barbero-Immirzi parameter γ. The computations are performed for many different values of the Barbero-Immirzi parameter γ, ranging from small to large. The resulting $\mathcal{S}(\vec{l})$ are compared with the Regge action on the double-Δ_3 complex. $\mathcal{S}(\vec{l})$ is well-approximated by the classical Regge action in the small-γ regime, and $\mathcal{S}(\vec{l})$ provides the correction to the Regge action with increasing γ. The solutions of the effective dynamics are computed numerically for different values of γ and compared to the solution of Regge equation. The solution from $\mathcal{S}(\vec{l})$ well-approximates the Regge solution for small γ and gives larger correction when increasing γ. Recovering the classical Regge action and solution from the effective dynamics of spinfoam amplitude gives evidence of the semiclassical consistency of spinfoam quantum gravity.

Recovering the classical Regge gravity from the spinfoam amplitude with small γ has been argued earlier in [15–20]. Our numerical result confirms this property for the spinfoam amplitude on the double-Δ_3 complex.

The numerical computations are performed for different γ's ranging from small to large. Fixing the boundary data, the solutions of the effective dynamics give a trajectory in the space of Regge geometries parametrized by γ. The trajectory approaches the solution of the classical Regge equation for small γ as mentioned above. For large γ, the trajectory stablizes at the Regge geometry that is different from the classical Regge solution. It suggests that the effective theory for large γ differs significantly from the Regge gravity. The solutions both at small and large γ give nonsuppressed contributions to the spinfoam amplitude. In particular, the solutions for large γ violate the known bound $|\gamma \delta_h| \lesssim \lambda^{-1/2}$ [11–13] (δ_h is the deficit angle of the Regge geometry), which is valid for nonsuppressed contributions to the amplitude with finite and small γ.

Studying the complex critical points in the spinfoam amplitude closely relates to the recent progress in numerical studies of spinfoam amplitudes [21]. Given the complexity of the spinfoam amplitude, the complex critical point and the corresponding contribution to the spinfoam amplitude has to be computed numerically. The numerical analysis of complex critical points connects to the Lefschetz thimble and Monte Carlo computation for the spinfoam integral [22], because every complex critical point associates to an integration cycle known as Lefschetz thimble, and the integral on the Lefschetz thimble collects all contributions associated to the complex critical point. Another related numerical result is the semiclassical expansion of the spinfoam amplitude to the next-to-leading order from the stationary phase approximation [23]. We also would like to mention a few other numerical approaches for spinfoam quantum gravity, including the "sl2cfoam-next" code for the nonperturbative computation of the spinfoam amplitude [24–26], the effective spinfoam model [13,27], the hybrid algorithm [28], and the spinfoam renormalization [29,30], etc.

This paper is organized as follows: Section II gives a brief review of the integral representation of the EPRL spinfoam amplitude and the definition of the large-j regime. In Sec. III, we define the real and complex critical points and discuss the general formalism of deriving the effective dynamics of Regge geometry. Section IV studies the complex critical point of the four-simplex amplitude

and generalizes the large-j asymptotics to include the non-Regge boundary data. Section V revisits the known results on the spinfoam amplitude on Δ_3 complex as the preparation for analyzing the amplitude on the double-Δ_3 complex. Section VI discusses the complex critical point in the spinfoam amplitude on the double-Δ_3 complex and computes the effective action. Section VII discusses the numerical solution of the effective dynamics on the double-Δ_3 complex. In Sec. VIII, we conclude and discuss some outlooks.

II. SPINFOAM AMPLITUDE

A four-dimensional simplicial complex $\mathcal{K}$ contains 4-simplices v, tetrahedra e, triangles f, line segments, and points. The internal and boundary triangles are denoted by h and b (f is either h or b). The SU(2) spins $j_h, j_b \in \mathbb{N}_0/2$ are assigned to internal and boundary triangles h, b. The spins label the quanta of triangle areas. The LQG area spectrum indicates that the quantum area of triangle f is given by $\mathfrak{a}_f = 8\pi\gamma G\hbar\sqrt{j_f(j_f+1)}$ [31,32]. In the large-j regime, which we will focus on, the area spectrum gives $\mathfrak{a}_f \simeq 8\pi\gamma G\hbar j_f$, or $\mathfrak{a}_f \simeq \gamma j_f$ when we set the unit such that $8\pi G\hbar = 1$.

The Lorentzian EPRL spinfoam amplitude on $\mathcal{K}$ is given by summing over internal spins $\{j_h\}$,

$$A(\mathcal{K}) = \sum_{\{j_h\}} \prod_h \boldsymbol{d}_{j_h}^{|V(f)|+1} \int [\mathrm{d}g\mathrm{d}\mathbf{z}] e^{S(j_h, g_{ve}, \mathbf{z}_{vf}; j_b, \xi_{eb})}, \tag{2.1}$$

$$[\mathrm{d}g\mathrm{d}\mathbf{z}] = \prod_{(v,e)} \mathrm{d}g_{ve} \prod_{(v,f)} \mathrm{d}\Omega_{\mathbf{z}_{vf}}, \tag{2.2}$$

where $\boldsymbol{d}_{j_h} = 2j_h + 1$. The boundary states are SU(2) coherent states $|j_b, \xi_{eb}\rangle$ where $\xi_{eb} = u_{eb} \triangleright (1,0)^{\mathrm{T}}$, $u_{eb} \in \mathrm{SU}(2)$. j_b and ξ_{eb} are determined by the area and the 3-normal of the boundary triangle b. The summed/integrated variables are $g_{ve} \in \mathrm{SL}(2,\mathbb{C})$, $\mathbf{z}_{vf} \in \mathbb{CP}^1$, and j_h. $\mathrm{d}g_{ve}$ is the Haar measure on $\mathrm{SL}(2,\mathbb{C})$,

$$\mathrm{d}g = \frac{\mathrm{d}\beta\mathrm{d}\beta^*\mathrm{d}\gamma\mathrm{d}\gamma^*\mathrm{d}\delta\mathrm{d}\delta^*}{|\delta|^2}, \quad \forall\, g = \begin{pmatrix} \alpha & \beta \\ \gamma & \delta \end{pmatrix} \in \mathrm{SL}(2,\mathbb{C}), \tag{2.3}$$

and $\mathrm{d}\Omega_{\mathbf{z}_{vf}}$ is the scaling invariant measure on $\mathbb{CP}^1$,

$$\mathrm{d}\Omega_{\mathbf{z}_{vf}} = \frac{i}{2} \frac{(z_0\mathrm{d}z_1 - z_1\mathrm{d}z_0) \wedge (\bar{z}_0\mathrm{d}\bar{z}_1 - \bar{z}_1\mathrm{d}\bar{z}_0)}{\langle Z_{vef}, Z_{vef}\rangle \langle Z_{ve'f}, Z_{ve'f}\rangle}, \quad \forall\, \mathbf{z}_{vf} = (z_0, z_1)^{\mathrm{T}}, \tag{2.4}$$

where $Z_{vef} = g_{ve}^\dagger \mathbf{z}_{vf}$, $\langle\cdot,\cdot\rangle$ is the Hermitian inner product on $\mathbb{C}^2$, and $\mathbf{z}_{vf}$ is a 2-component spinor for the face f.

The spinfoam action S in Eq. (2.1) is complex and linear to j_h, j_b in an expression of the form [33],

$$S = \sum_{e'} j_h F_{(e',h)} + \sum_{(e,b)} j_b F^{\mathrm{in/out}}_{(e,b)} + \sum_{(e',b)} j_b F^{\mathrm{in/out}}_{(e',b)}, \tag{2.5}$$

$$F^{\mathrm{out}}_{(e,b)} = 2\ln \frac{\langle Z_{veb}, \xi_{eb}\rangle}{\|Z_{veb}\|} + i\gamma \ln \|Z_{veb}\|^2, \tag{2.6}$$

$$F^{\mathrm{in}}_{(e,b)} = 2\ln \frac{\langle \xi_{eb}, Z_{v'eb}\rangle}{\|Z_{v'eb}\|} - i\gamma \ln \|Z_{v'eb}\|^2, \tag{2.7}$$

$$F_{(e',f)} = 2\ln \frac{\langle Z_{ve'f}, Z_{v'e'f}\rangle}{\|Z_{ve'f}\|\|Z_{v'e'f}\|} + i\gamma \ln \frac{\|Z_{ve'f}\|^2}{\|Z_{v'e'f}\|^2}. \tag{2.8}$$

Here, e and e' are boundary and internal tetrahedra, respectively. In the dual complex $\mathcal{K}^*$, the orientation of ∂f^* is outgoing from the vertex dual to v and incoming to another vertex dual to v', and the orientation of the face f^* dual to f induces ∂f^*'s orientation. As for the logarithms in the spinfoam action, we fix all the logarithms to be the principal values. The derivation of the spinfoam action S is given in [33].

The spinfoam amplitude in the formulation (2.1) has the following three types of continuous gauge degrees of freedom, and thus some gauge fixings are needed to remove the redundant degrees of freedom:

(i) Firstly, there is $\mathrm{SL}(2,\mathbb{C})$ gauge transformation at each v:

$$g_{ve} \mapsto x_v^{-1} g_{ve}, \quad \mathbf{z}_{vf} \mapsto x_v^\dagger \mathbf{z}_{vf}, \quad x_v \in \mathrm{SL}(2,\mathbb{C}). \tag{2.9}$$

To remove this gauge degree of freedom, we fix one g_{ve} to be a constant $\mathrm{SL}(2,\mathbb{C})$ matrix for each four-simplex. The amplitude is independent of the choices of constant matrices.

(ii) Secondly, there is SU(2) gauge transformation on each internal e:

$$g_{v'e} \mapsto g_{v'e} h_e^{-1}, \quad g_{ve} \mapsto g_{ve} h_e^{-1}, \quad h_e \in \mathrm{SU}(2). \tag{2.10}$$

To fix this SU(2) gauge freedom, one can parameterize one of two $\mathrm{SL}(2,\mathbb{C})$ elements: g_{ve}, or $g_{v'e}$ by the upper triangular matrix

$$k = \begin{pmatrix} \lambda^{-1} & \mu \\ 0 & \lambda \end{pmatrix}, \quad \lambda \in \mathbb{R}\backslash\{0\}, \quad \mu \in \mathbb{C} \tag{2.11}$$

Here, we use the fact that any $g \in \mathrm{SL}(2,\mathbb{C})$ can be decomposed as $g = kh$ with $h \in \mathrm{SU}(2)$ and k an upper triangular matrix in Eq. (2.11).

(iii) Thirdly, for each $\mathbf{z}_{vf}$, there is the scaling gauge freedom:

$$\mathbf{z}_{vf} \mapsto \lambda_{vf} \mathbf{z}_{vf}, \qquad \lambda_{vf} \in \mathbb{C}. \tag{2.12}$$

Here, we fix the gauge by setting the first component of $\mathbf{z}_{vf}$ to 1, i.e. $\mathbf{z}_{vf} = (1, \alpha_{vf})^{\mathrm{T}}$, where $\alpha_{vf} \in \mathbb{C}$.

Furthermore, in Eq. (2.1), we assume the summation over internal $j_h \in \mathbb{N}_0/2$ is bounded by $j^{\max}$. In some situations, $j^{\max}$ is determined by boundary spins j_b via the triangle inequality, otherwise $j^{\max}$ are imposed as the cutoff to regularize the infinite sum over spins. To prepare for the stationary phase analysis, we would like to change the summation over j_h in Eq. (2.1) to integrals. The idea is to apply the Poisson summation formula. Firstly, we replace each $\boldsymbol{d}_{j_h}$ by a smooth compact support function $\tau_{[-\epsilon,j^{\max}+\epsilon]}(j_h)$ satisfying

$$\tau_{[-\epsilon,j^{\max}+\epsilon]}(j_h) = \boldsymbol{d}_{j_h}^{|V(f)|+1}, \quad \text{for } j_h \in [0, j^{\max}], \quad \text{and}$$
$$\tau_{[-\epsilon,j^{\max}+\epsilon]}(j_h) = 0, \quad \text{for } j_h \notin [-\epsilon, j^{\max}+\epsilon],$$

for any $0 < \epsilon < 1/2$. This replacement does not change the value of the amplitude $A(\mathcal{K})$ but makes the summand of $\sum_{j_h}$ smooth and compact support in j_h. Then, by applying the Poisson summation formula,

$$\sum_{n\in\mathbb{Z}} f(n) = \sum_{k\in\mathbb{Z}} \int_{\mathbb{R}} \mathrm{d}n f(n) e^{2\pi i k n},$$

the discrete summation over j_h in Eq. (2.1) becomes the summing of integrals:

$$A(\mathcal{K}) = \sum_{\{k_h\in\mathbb{Z}\}} \int \prod_h \mathrm{d}j_h \prod_h 2\tau_{[-\epsilon,j^{\max}+\epsilon]}(j_h) \int [\mathrm{d}g\mathrm{d}\mathbf{z}] e^{S^{(k)}}, \tag{2.13}$$

$$S^{(k)} = S + 4\pi i \sum_h j_h k_h. \tag{2.14}$$

By the area spectrum, the classical area $\mathfrak{a}_f$ and small $\hbar$ imply the large spin $j_f \gg 1$. This motivates understanding the large-j regime as the semiclassical regime of $A(\mathcal{K})$. Then, to probe the semiclassical regime, we scale uniformly both the boundary spins j_b and the internal spin cutoff $j^{\max}$ by

$$j_b \to \lambda j_b, \qquad j^{\max} \to \lambda j^{\max}, \qquad \lambda \gg 1, \tag{2.15}$$

so $S \to \lambda S$ as a result from S being linear in j_b, j_h. As a consequence, the spinfoam amlitude $A(\mathcal{K})$ in the large-j regime is

$$A(\mathcal{K}) = \sum_{\{k_h\in\mathbb{Z}\}} \int_{\mathbb{R}} \prod_h \mathrm{d}j_h \prod_h 2\lambda\tau_{[-\epsilon,\lambda j^{\max}+\epsilon]}(\lambda j_h) \times \int [\mathrm{d}g\mathrm{d}\mathbf{z}] e^{\lambda S^{(k)}}, \tag{2.16}$$

$$S^{(k)} = S + 4\pi i \sum_h j_h k_h, \tag{2.17}$$

by the change of integration variables $j_h \to \lambda j_h$, and j_h is continous.

III. COMPLEX CRITICAL POINT AND EFFECTIVE DYNAMICS

The integral in (2.16) at each k_h can be analyzed with the stationary phase method in the regime $\lambda \gg 1$. By the standard argument of the stationary phase approximation, by fixing the boundary data, the integral with $\lambda \gg 1$ is approximated by the dominant contributions from the solutions of critical equations and neighborhood. In the case of the integrals in (2.16), the critical equations are

$$\mathrm{Re}(S) = \partial_{g_{ve}} S = \partial_{\mathbf{z}_{vf}} S = 0, \tag{3.1}$$

$$\partial_{j_h} S = 4\pi i k_h, \qquad k_h \in \mathbb{Z}. \tag{3.2}$$

The solutions inside the integration domain are denoted by $\{\overset{\circ}{j}_h, \overset{\circ}{g}_{ve}, \overset{\circ}{\mathbf{z}}_{vf}\}$. The integration domain is viewed as a real manifold, and the integration variables are real and imaginary parts of the matrix elements in g_{ve} and $\mathbf{z}_{vf}$. We call $\{\overset{\circ}{j}_h, \overset{\circ}{g}_{ve}, \overset{\circ}{\mathbf{z}}_{vf}\}$ the real critical point accordingly.

The existence of the real critical point in (2.16) depends on the boundary condition. The real critical point may not exist for the generic boundary condition. We know that S is a complex action with n real variables x, and $\partial_x S = 0$ gives n complex thus $2n$ real equations, which is overconstrained for n real variables. Consequently, the critical equations (3.1) and (3.2) coupled with one more equation $\mathrm{Re}(S) = 0$ result in the nonexistence of the general real solution, unless for some special boundary conditions.

As a solution to this problem of overconstrained equations, the integration variables have to be complexified, and action S has to be analytically continued to the complex variables z. We are only interested in the integration domain where the spinfoam action S is analytic. The analytically continued action is denoted by $\mathcal{S}$. On the space of complex variables, the complex critical equation $\partial_z \mathcal{S} = 0$ is not overconstrained anymore because it gives n complex equations for n complex variables. $\mathrm{Re}(S) = 0$ is dropped when we study $\mathcal{S}$ instead of S. In the space of complex variables, the solutions of $\partial_z \mathcal{S} = 0$ are called the complex critical points, which play the dominant role for the asymptotics of $A(\mathcal{K})$ in the case that the real critical point is absent.

Before discussing the complex critical point, let us firstly review some known results from the critical equations (3.1) and (3.2) with the boundary data corresponding to Regge geometry on $\partial\mathcal{K}$. The real solutions of the part (3.1) have been well-studied in the literature [7–9,33]. We call these solutions the pseudocritical points. As one of the results, the pseudocritical point satisfying a nondegeneracy condition endows a Regge geometry on $\mathcal{K}$ with certain four-simplex orientations. When focusing on the pseudocritical

points endowing the uniform orientations to all four-simplices, further imposing (3.2) to them gives the accidental flatness constraint to their corresponding Regge geometries, i.e., every deficit angle δ_h hinged by the internal triangle h [11,34] satisfies

$$\gamma\delta_h = 4\pi k_h, \qquad k_h \in \mathbb{Z}. \tag{3.3}$$

When $k_h = 0$, δ_h at every internal triangle is zero, and the Regge geometry endowed by the real critical point is flat. Equation (3.3) is a strong constraint to the allowed geometry from the spinfoams and can be satisfied only for special boundary conditions that admit the flat bulk geometry (mod $4\pi\mathbb{Z}$). The accidental flatness constraint is consistent with the above argument about overconstrained equations, and it has been demonstrated explicitly in the example well-studied in, e.g., [12,35]. If one only considers the real critical point for the dominant contribution to $A(\mathcal{K})$, Eq. (3.3) would imply that only the flat geometry (mod $4\pi\mathbb{Z}$) exists. This confusion leading to the flatness problem results from ignoring the complex critical point in the stationary phase analysis.

In the following discussion, we show that the large-λ spinfoam amplitude does receive dominant contributions from the complex critical points away from the real integration domain. The complex critical points precisely correspond to the curved Regge geometries emergent from the spinfoam amplitude. Interestingly, the application of complex critical points leads to a derivation of effective dynamics of Regge geometry from the spinfoam amplitude. The emergent curved Regge geometries are constrained by the effective dynamics. We firstly provide a general formalism below, then we apply the formalism to the concrete models with several different $\mathcal{K}$ in the following sections.

Motivated by relating to the dynamics of Regge geometry, we separate the integral in the amplitude (2.16) into two parts. Suppose $\mathcal{K}$ has M internal segments, the dynamics of Regge geometry should relate to the dynamics of these internal segment lengths. Motivated by this, we separate M internal areas j_{h_o} ($h_o = 1, \ldots, M$) from other $j_{\bar{h}}$ ($\bar{h} = 1, \ldots, F - M$), where j_{h_o} relates to the segment lengths. Here, F is the total number of internal triangles in $\mathcal{K}$, and M equals the number of the separated internal segments. The spinfoam amplitude (2.16) then becomes

$$A(\mathcal{K}) = \sum_{\{k_h\}} \int \prod_{h_o=1}^{M} \mathrm{d}j_{h_o} \mathcal{Z}_{\mathcal{K}}^{\{k_h\}}(j_{h_o}), \tag{3.4}$$

where $\mathcal{Z}_{\mathcal{K}}^{\{k_h\}}$, called the partial amplitude, is given by

$$\mathcal{Z}_{\mathcal{K}}^{\{k_h\}}(j_{h_o}) = \int \prod_{\bar{h}} \mathrm{d}j_{\bar{h}} \prod_{h} (2\lambda \boldsymbol{d}_{\lambda j_h}) \int [\mathrm{d}g\mathrm{d}\mathbf{z}] e^{\lambda S^{(k)}}. \tag{3.5}$$

We can then change variables from the areas j_{h_o} to the internal segment-lengths $\{l_I\}_{I=1}^M$, with I denoting the internal segment. The internal triangles $h_o = 1, \ldots, M$ are suitably chosen such that the change of variables is well-defined in the interested region, e.g., a neighborhood of $\{\overset{\circ}{j}_{h_o}\}$ of $\{\overset{\circ}{j}_h, \overset{\circ}{g}_{ve}, \overset{\circ}{\mathbf{z}}_{vf}\}$ corresponding to the flat geometry. Indeed, the chosen M areas $\{j_{h_o}\}$ are related to M segment lengths $\{l_I\}$ by Heron's formula. Inverting the relation between $\{j_{h_o}\}_{h_o=1}^M$ and $\{l_I\}_{I=1}^M$ defines the local change of variables $(j_{h_o}, j_{\bar{h}}) \to (l_I, j_{\bar{h}})$ in a neighborhood K of a given Regge geometry in the integration domain of (2.16). This procedure is just changing variables without imposing any restrictions. When focusing on the integrals in the neighborhood K, we have $\mathrm{d}^{M+N} j_h = \mathcal{J}_l \mathrm{d}^M l_I \mathrm{d}^{F-M} j_{\bar{h}}$, where $\mathcal{J}_l = \det(\partial j_{h_o}/\partial l_I)$ is the Jacobian obtained by the derivatives of Heron's formula. Therefore, the contribution to $A(\mathcal{K})$ from the neighborhood K is expressed as

$$\sum_{\{k_h\}} \int \prod_{I=1}^{M} \mathrm{d}l_I \mathcal{J}_l \mathcal{Z}_{\mathcal{K}}^{\{k_h\}}(l_I), \tag{3.6}$$

The partial amplitude $\mathcal{Z}_{\mathcal{K}}^{\{k_h\}}$ has the external parameters $r \equiv \{l_I, j_b, \xi_{eb}\}$ including not only the boundary data j_b, ξ_{eb} but also internal segment-lengths l_I. The above decomposition of j_h integrals closely relates to the earlier proposal [36,37] (see also [38] in the context of area Regge calculus). l_I parametrizes a submanifold $\mathcal{M}_{\mathrm{Regge}}$ in the space of j_h. The submanifold $\mathcal{M}_{\mathrm{Regge}}$ collects j_h's that can be interpreted as areas determined by the segment lengths l_I (by Heron's formula). Generically, the space of j_h is much larger than the space of segment lengths [39]. $j_{\bar{h}}$ parametrizes the direction transverse to $\mathcal{M}_{\mathrm{Regge}}$.

To study the partial amplitude $\mathcal{Z}_{\mathcal{K}}^{\{k_h\}}$, we apply the theory of stationary phase approximation for complex action with parameters [40,41]. In the following, we only consider the partial amplitude with $k_h = 0$, while the situation with other k_h can be studied analogously. We consider the large-λ integral $\int_K e^{\lambda S(r,x)} \mathrm{d}^N x$, and regard r as the external parameters. $S(r, x)$ is an analytic function of $r \in U \subset \mathbb{R}^k, x \in K \subset \mathbb{R}^N$. $U \times K$ is a neighborhood of $(\overset{\circ}{r}, \overset{\circ}{x})$, where $\overset{\circ}{x}$ is a real critical point of $S(\overset{\circ}{r}, x)$. $\mathcal{S}(r, z)$ with $z = x + iy \in \mathbb{C}^N$ is the analytic extension of $S(r, x)$ to a complex neighborhood of $\overset{\circ}{x}$. The complex critical equation is

$$\partial_z \mathcal{S} = 0, \tag{3.7}$$

whose solution is $z = Z(r)$. Here, $Z(r)$ is an analytic function of r in the neighborhood U. When $r = \overset{\circ}{r}, Z(\overset{\circ}{r}) = \overset{\circ}{x}$ reduces to the real critical point. When r deviates away from $\overset{\circ}{r}$, $Z(r) \in \mathbb{C}^N$ can move away from the real plane $\mathbb{R}^N$, thus it is called the complex critical point (see Fig. 1). With

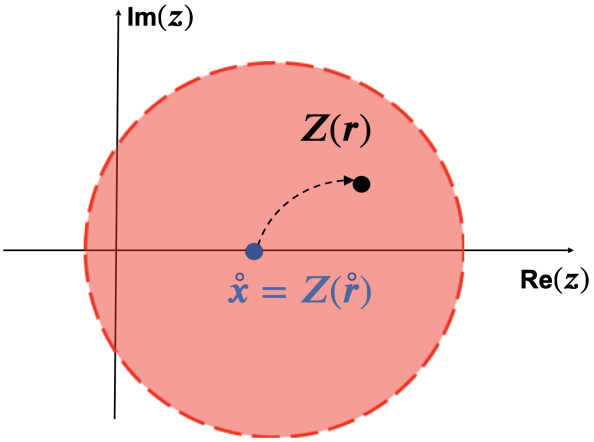

FIG. 1. The real and complex critical points $\mathring{x}$ and $Z(r)$. $\mathcal{S}(r,z)$ is analytic extended from the real axis to the complex neighborhood illustrated by the red disk.

this in mind, we have the following large-λ asymptotic expansion for the integral

$$\int_K e^{\lambda S(r,x)} \mathrm{d}^N x = \left(\frac{1}{\lambda}\right)^{\frac{N}{2}} \frac{e^{\lambda \mathcal{S}(r,Z(r))}}{\sqrt{\det\left(-\partial^2_{z,z}\mathcal{S}(r,Z(r))/2\pi\right)}} \times [1 + O(1/\lambda)], \tag{3.8}$$

where $\mathcal{S}(r,Z(r))$ and $\delta^2_{z,z}\mathcal{S}(r,Z(r))$ are the action and Hessian at the complex critical point. In addition, the real part of $\mathcal{S}$ is zero or negative. More precisely, there exists a constant $C > 0$ such that

$$\mathrm{Re}(\mathcal{S}) \le -C|\mathrm{Im}(Z)|^2. \tag{3.9}$$

See [40,41] for the proof of this inequality. This inequality indicates that $\mathrm{Re}(\mathcal{S}) = 0$ resulting in the oscillatory phase in (3.8) can only happen at the real critical point, where $\mathrm{Im}(Z) = 0$ and $r = \mathring{r}$. When r deviates from $\mathring{r}$ with a finite distance, such that $\mathrm{Im}(Z)$ is finite and $\mathrm{Re}(\mathcal{S})$ is negative, (3.8) is exponentially suppressed when scaling λ to large. The asymptotic formula (3.8) depends analytically on r and interpolates the two different behaviors smoothly in the parameter space of r:

(i) The critical point is not real, then $\mathrm{Re}(\mathcal{S}) < 0$, which gives the exponentially decaying amplitude.
(ii) The critical point is real, then $\mathrm{Re}(\mathcal{S}) = 0$, and thus $e^{\lambda\mathcal{S}}$ gives an oscillatory phase.

These two distinct behaviors are obtained by fixing r and scaling λ. But since the asymptotic formula (3.8) depends on r analytically, we can vary r simultaneously as scaling λ. Then we can arrive at the regime where the asymptotic behavior (3.8) is not suppressed at the complex critical point. Indeed, for any large λ, there always exists $r \neq \mathring{r}$ but sufficiently close to $\mathring{r}$, such that $\mathrm{Im}(Z)$ and $\mathrm{Re}(\mathcal{S})$ are small enough, then $e^{\lambda\mathcal{S}}$ in (3.8) is not suppressed at the complex critical point.

The importance of (3.8) is that the integral can receive a dominant contribution from the complex critical point away from the real plane. These complex critical points indeed give the curved Regge geometries missing in the argument of the flatness problem. The parameter r including both the boundary data and internal segment lengths determine the Regge geometry that is generically curved. Hence the asymptotic formula (3.8) computes the weight of the Regge geometry contributing to the amplitude and reduces $A(\mathcal{K})$ in K to

$$\left(\frac{1}{\lambda}\right)^{\frac{N}{2}} \int \prod_{I=1}^{M} \mathrm{d}l_I \mathcal{N}_l e^{\lambda \mathcal{S}(r,Z(r))}[1 + O(1/\lambda)] \tag{3.10}$$

at each k_h. Here, $\mathcal{N}_l \propto \prod_h (4j_h)\mathcal{J}_l[\det(-\delta^2_{z,z}\mathcal{S}/2\pi)]^{-1/2}$ at $Z(r)$, and $r = \{l_I, j_b, \xi_{eb}\}$. Given that $\{l_I\}$ determines the Regge geometry on $\mathcal{K}$, Eq. (3.10) is a path integral of Regge geometries with the effective action $\mathcal{S}$. The integration domain of l_I includes curved geometries. The integral (3.10) derived from the spinfoam amplitude defines an effective theory of Regge geometries. Indeed, if we focus on the dominant contribution and neglect corrections of $O(1/\lambda)$, by the stationary phase approximation of (3.10), the effective action $\mathcal{S}$ gives the equation of motion

$$\frac{\partial \mathcal{S}}{\partial l_I} = 0, \qquad I = 1, \ldots, M, \tag{3.11}$$

which determines the effective dynamics of Regge geometry. $\mathcal{S}$ is generally complex, so (3.11) should be analytically continued to complex l_I, and thus the solution is generally not real. As we are going to see in Sec. VII, we are mainly interested in the regime where the imaginary part of the solution l_I is negligible, then the solution has the interpretation of the Regge geometry.

In the following, we make the above general analysis concrete by considering the examples of spinfoam amplitudes on a single four-simplex and the double-Δ_3 complex. We also revisit briefly the existing results on Δ_3 complex for the completeness. We compute numerically the complex critical points and $\mathcal{S}$, confirming the contribution of the complex critical points to the spinfoam amplitude. In particular, the double-Δ_3 model corresponding to $M = 1$ exhibits the nontrivial effective dynamics of the Regge geometries. The effective dynamics approximates the classical Regge calculus in the small-γ regime.

IV. FOUR-SIMPLEX AMPLITUDE

This section applies the above general procedure to the simplest situation—the four-simplex amplitude. In this

case, there is no internal triangle as $F = M = 0$. The external parameter r only contains the boundary data $r = (j_b, \xi_{eb})$. The four-simplex and its dual diagram are illustrated in Figs. 2(a) and 2(b). The points of the four-simplex v are labeled by (1, 2, 3, 4, 5). The five tetrahedra on the boundary are labeled by

$$\{e_1, e_2, e_3, e_4, e_5\} = \{(1,2,3,4),(1,2,3,5),(1,2,4,5),(1,3,4,5),(2,3,4,5)\}.$$

These tetrahedra carry group variable $g_{ve} \in \mathrm{SL}(2,\mathbb{C})$. The triangle is shared by the tetrahedra and carries an SU(2) spin j_f, e.g., the tetrahedron $e_1 = (1,2,3,4)$ and the tetrahedron $e_2 = (1,2,3,5)$ share the face $f_1 = (1,2,3)$.

A. The amplitude and parametrization of variables

According to (2.1), the EPRL four-simplex amplitude with the boundary state has the following expression [7–9,42–44]:

$$A_v(j_f, \xi_{ef}) = \int \prod_e \mathrm{d}g_{ve}\delta_{i\sigma_3}(g_{ve_1}) \int_{(\mathbb{CP}^1)^{10}} e^S \prod_f \frac{d_{j_f}}{\pi} \mathrm{d}\Omega_{\mathbf{z}_{vf}}. \tag{4.1}$$

Here, all triangles are on the boundary, $j_f = j_b$. To fix the $\mathrm{SL}(2,\mathbb{C})$ gauge, g_{ve_1} is fixed to be constant matrix $\mathrm{diag}(i,-i)$ (the timelike normal of the reference tetrahedron e_1 is past-pointing). The integrand in (4.1) is written as an exponential e^S with the action

$$S = \sum_f 2j_f \ln \frac{\langle \xi_{ef}, Z_{vef}\rangle \langle Z_{ve'f}, \xi_{e'f}\rangle}{\|Z_{vef}\|\|Z_{ve'f}\|} + i\gamma j_f \ln \frac{\langle Z_{ve'f}, Z_{ve'f}\rangle}{\langle Z_{vef}, Z_{vef}\rangle}. \tag{4.2}$$

The orientations of dual faces follow from Fig. 2(c). To study the large-j behavior of the amplitude, we scale all boundary spins $j_f \to \lambda j_f$ by the parameter $\lambda \gg 1$. The scaling of spins results in the scaling of action $S \mapsto \lambda S$, such that the integral (4.1) can be studied by the stationary phase approximation. In the following, we firstly compute the real critical point $\{\mathring{g}_{ve}, \mathring{z}_{vf}\}$, which is the solution of the critical equation (3.1) and then describe the algorithm to compute the complex critical point in the neighborhood.

To obtain the real critical point, we adopt the four-simplex geometry used in [22,23,45] to generate the boundary state. The coordinates of the five vertices P_a in Fig. 2(a) in the Minkowski spacetime are set as

$$\begin{aligned} P_1 &= (0,0,0,0), \qquad P_2 = (0,0,0,-2\sqrt{5}/3^{1/4}),\\ P_3 &= (0,0,-3^{1/4}\sqrt{5},-3^{1/4}\sqrt{5}),\\ P_4 &= (0,-2\sqrt{10}/3^{3/4},-\sqrt{5}/3^{3/4},-\sqrt{5}/3^{1/4}),\\ P_5 &= (-3^{-1/4}10^{-1/2},-\sqrt{5/2}/3^{3/4},-\sqrt{5}/3^{3/4},-\sqrt{5}/3^{1/4}). \end{aligned} \tag{4.3}$$

Then, the 4D normals of the tetrahedra are

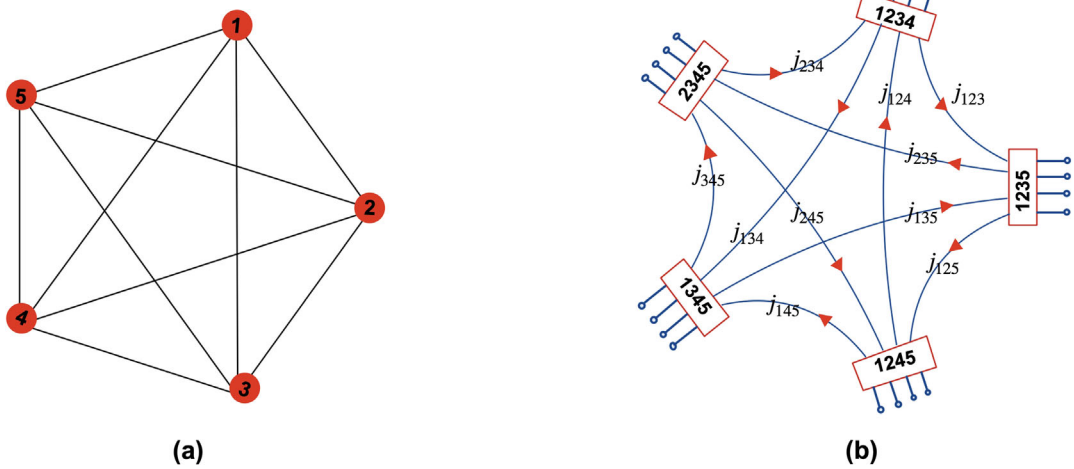

FIG. 2. Panel (a) plots the four-simplex $v = (1,2,3,4,5)$. The boundary comprises five tetrahedra e_i sharing ten faces f_i [The shared faces are labeled by $\{f_1, f_2, \ldots, f_{10}\} = \{(1,2,3),(1,2,4),(1,2,5),(1,3,4),(1,3,5),(2,3,4),(2,3,5),(3,4,5)\}$. For convenience, in this section, the notations e and f mean that $e \in \{e_1, \ldots, e_5\}$ and $f \in \{f_1, \ldots, f_{10}\}$]. Panel (b) is the dual complex of the four-simplex. Five boxes correspond to boundary tetrahedra carrying $g_{ve} \in \mathrm{SL}(2,\mathbb{C})$. The strands correspond to triangles carrying spins j_f. The circles as endpoints of strands carry boundary states ξ_{ef}. The arrows represent the orientations of strands.

$$N_{e_1} = (-1,0,0,0), \qquad N_{e_2} = \left(\frac{5}{\sqrt{22}}, \sqrt{\frac{3}{22}}, 0, 0\right),$$
$$N_{e_3} = \left(\frac{5}{\sqrt{22}}, -\frac{1}{\sqrt{66}}, \frac{2}{\sqrt{33}}, 0\right),$$
$$N_{e_4} = \left(\frac{5}{\sqrt{22}}, -\frac{1}{\sqrt{66}}, -\frac{1}{\sqrt{33}}, \frac{1}{\sqrt{11}}\right),$$
$$N_{e_5} = \left(\frac{5}{\sqrt{22}}, -\frac{1}{\sqrt{66}}, -\frac{1}{\sqrt{33}}, -\frac{1}{\sqrt{11}}\right). \tag{4.4}$$

The spinor ξ_{ef} relates to the 3D normals n_{ef} by $n_{ef} = \langle \xi_{ef}, \vec{\sigma}\xi_{ef}\rangle$ ($\vec{\sigma}$ are Pauli matrices). The Regge boundary data of ten areas $\mathring{j}_f$, 3D normals $\mathring{n}_{ef}$ and the corresponding spinors $\mathring{\xi}_{ef}$ of the four-simplex are listed in Appendix A.

With the Lorentzian-Regge boundary data $\mathring{r} = (\mathring{j}_f, \mathring{\xi}_{ef})$, we solve for the real critical point $(\mathring{g}_{ve}, \mathring{\mathbf{z}}_{vf})$ which satisfies $\mathrm{Re}(S) = \partial_{g_{ve}} S = \partial_{z_{vf}} S = 0$. The results in the literature [8,9] show that there are exactly two real critical points, which have the interpretations as the geometrical four-simplex with opposite four-orientations. The four-simplex geometrical interpretation of the critical points results in the same geometry as the one given by (4.3). We compute the real critical point following the strategy described in [12,14,45], where the boundary data and critical points for a single four-simplex are studied in detail. The data of the real critical point $(\mathring{g}_{ve}, \mathring{\mathbf{z}}_{vf})$ is given in Appendix A.

By fixing the rescaling gauge of $\mathbf{z}_{vf}$, each $\mathbf{z}_{vf}$ can be parametrized with two real variables x_{vf}, y_{vf},

$$\mathbf{z}_{vf} = (1, x_{vf} + \mathrm{i}y_{vf})^{\mathrm{T}}. \tag{4.5}$$

$g_{ve_i}, i = (2,3,4,5)$ are parametrized as

$$\begin{pmatrix} 1 + (x^1_{ve} + \mathrm{i}y^1_{ve})/\sqrt{2} & (x^2_{ve} + \mathrm{i}y^2_{ve})/\sqrt{2} \\ (x^3_{ve} + \mathrm{i}y^3_{ve})/\sqrt{2} & \frac{1+(x^2_{ve}+\mathrm{i}y^2_{ve})(x^3_{ve}+\mathrm{i}y^3_{ve})/2}{1+(x^1_{ve}+\mathrm{i}y^1_{ve})/\sqrt{2}} \end{pmatrix},$$
$$x^1_{ve}, y^1_{ve}, x^2_{ve}, y^2_{ve}, x^3_{ve}, y^3_{ve} \in \mathbb{R}. \tag{4.6}$$

Therefore, the four-simplex action is a function in terms of all real variables $x = (x_{vf}, y_{vf}, x^1_{ve}, y^1_{ve}, x^2_{ve}, y^2_{ve}, x^3_{ve}, y^3_{ve})$ for all f in $\{f_1, \ldots f_{10}\}$ and e in $\{e_2, ..e_5\}$. The real critical point $\mathring{\mathbf{z}}_{vf}$ is in the form $\mathring{\mathbf{z}}_{vf} = (1, \mathring{\alpha}_{vf})^T$, where $\mathring{\alpha}_{vf} = \mathring{x}_{vf} + \mathrm{i}\mathring{y}_{vf} \in \mathbb{C}$. It is convenient to set one of the critical points at the origin $\mathring{x} = \{0, 0, \ldots, 0\}$ by modifying (4.5) and (4.6) to

$$\mathbf{z}_{vf} = (1, \mathring{\alpha}_{vf} + x_{vf} + \mathrm{i}y_{vf})^{\mathrm{T}},$$
$$g_{ve} = \mathring{g}_{ve} \begin{pmatrix} 1 + (x^1_{ve} + \mathrm{i}y^1_{ve})/\sqrt{2} & (x^2_{ve} + \mathrm{i}y^2_{ve})/\sqrt{2} \\ (x^3_{ve} + \mathrm{i}y^3_{ve})/\sqrt{2} & \frac{1+(x^2_{ve}+\mathrm{i}y^2_{ve})(x^3_{ve}+\mathrm{i}y^3_{ve})/2}{1+(x^1_{ve}+\mathrm{i}y^1_{ve})/\sqrt{2}} \end{pmatrix}. \tag{4.7}$$

With the parametrization in (4.7), the measures $\mathrm{d}g_{ve}$ and $\mathrm{d}\Omega_{\mathbf{z}_{vf}}$ are

$$\mathrm{d}g_{ve} = \frac{1}{128\pi^4} \frac{\mathrm{d}x^1_{ve}\mathrm{d}x^2_{ve}\mathrm{d}x^3_{ve}\mathrm{d}y^1_{ve}\mathrm{d}y^2_{ve}\mathrm{d}y^3_{ve}}{\left|1 + \frac{x^1_{ve}+\mathrm{i}y^1_{ve}}{\sqrt{2}}\right|^2},$$
$$\mathrm{d}\Omega_{\mathbf{z}_{vf}} = \frac{\mathrm{d}x_{vf}\mathrm{d}y_{vf}}{\langle Z_{vef}, Z_{vef}\rangle \langle Z_{ve'f}, Z_{ve'f}\rangle}. \tag{4.8}$$

As a result, the four-simplex amplitude is in the form

$$A_v = \int \mathrm{d}^{44}x \mu(x) e^{\lambda S(r,x)}, \tag{4.9}$$

where $r = (j_f, \xi_{ef})$ are boundary data. The integral is 44 real-dimensional. In the following, we focus on a neighborhood K of $\mathring{x}$. We have defined the local coordinates $x \in \mathbb{R}^{44}$ covering K.

B. Deviating from the shape matching

The amplitude A_v has the real critical points with the nondegenerate Regge boundary data $\mathring{r}$. However, the real critical point disappears when the boundary data deviates away from $\mathring{r}$. Considering a neighborhood U of $\mathring{r}$ in the space of boundary data, such that any $r \in U$ (different from $\mathring{r}$) does not correspond to any Regge geometry or vector geometry.[1] If we fix $r \in U$ and scale the spins with a large λ, there are two possible behaviors for the amplitude [8,43]:

(i) For $r = \mathring{r}$, the amplitude has two critical points whose geometrical interpretations have opposite orientations. S evaluated at critical points gives the Regge action of the 4-simplex with opposite sign. Therefore, the asymptotic amplitude of the four-simplex gives two oscillatory phases

$$A_v \simeq \lambda^{-12}(N_+ e^{i\lambda S_{\mathrm{Regge}}} + N_- e^{-i\lambda S_{\mathrm{Regge}}}). \tag{4.10}$$

(ii) For $r \neq \mathring{r}$, it leads to no solutions to (3.1) and the exponentially suppressed amplitude.

To interpolate smoothly between the oscillatory phases and the exponential suppression in the asymptotics (4.10), the

[1]In the Lorentzian EPRL spinfoam amplitude, the critical points corresponding to the nondegenerate Regge geometry are isolated critical points.

discussion in Sec. III suggests making r vary and introducing the complex critical points.

The boundary data $\mathring{r} = \{\mathring{j}_f, \mathring{\xi}_{ef}\}$ of the Lorentzian Regge geometry satisfies the shape-matching condition, i.e., five geometrical tetrahedra determined by $\mathring{r}$ on the boundary are glued with the triangles matching in shapes. Consider the four-simplex action $S(r,x)$ in the neighborhood $K \times U$ of $(\mathring{r}, \mathring{x})$. We define $z \in \mathbb{C}^{44}$ as the complexification of x, and $\mathcal{S}(r,z)$ extends holomorphically $S(r,x)$ to a complex neighborhood of $\mathring{x}$. To avoid confusion, we note that the integration variables x are complexified, while the boundary data $r = (j_f, \xi_{ef})$ is real.

Next, we let $r = \mathring{r} + \delta r$ vary, such that the shape-matching condition violates. We describe below a parametrization of the tetrahedron shapes. A tetrahedron in $\mathbb{R}^3$ is determined by four points $\{\tilde{P}_a, \tilde{P}_b, \tilde{P}_c, \tilde{P}_d\}$ up to a $\mathbb{R}^3 \rtimes \mathrm{O}(3)$ symmetry. We gauge fix the $\mathbb{R}^3 \rtimes \mathrm{O}(3)$ symmetry by choosing $\tilde{P}_a$ at the origin, $\tilde{P}_b$ along the z axis, and $\tilde{P}_c$ within the (y,z)-plane. The last point $\tilde{P}_d$ is not constrained. Given the tetrahedron's segment lengths, the coordinates of the points are fixed in $\mathbb{R}^3$ by the above gauge fixing. For example, for the tetrahedron $e_2 = \{1,2,3,5\}$, $\mathring{r}$ implies that the coordinates of the points in $\mathbb{R}^3$ are given by

$$\begin{aligned}
&\tilde{P}_1 = (0,0,0), \qquad \tilde{P}_2 = (0,0,-3.40),\\
&\tilde{P}_3 = (0,-2.94,-1.70),\\
&\tilde{P}_5 = (-0.651,-0.981,-1.70).
\end{aligned} \tag{4.11}$$

All other four tetrahedra can be described similarly, and the coordinates of the points in $\mathbb{R}^3$ are determined by $\mathring{r}$. The 3D face-normals $\vec{n}$ implied by the coordinates match with the data in Table III up to a simultaneous SO(3) rotation. The spinors ξ associating with each face are given by

$$\xi = \frac{1}{\sqrt{2}}\left(\sqrt{1+w}, \frac{x+\mathrm{i}y}{\sqrt{1+w}}\right)^{\mathrm{T}}, \quad \text{if } \vec{n} = (x,y,w)^{\mathrm{T}}. \tag{4.12}$$

When we deform the boundary data, we keep the areas $j_f = \mathring{j}_f$ unchanged, while ξ_{ef} are deformed, such that the boundary data r is deformed to violate the shape-matching condition. We move the vertices $\tilde{P}_a \in \mathbb{R}^3$ to deform the tetrahedron shapes. For example, the vertices in (4.11) are moved to new positions

$$\begin{aligned}
&\tilde{P}_1 = (0,0,0), \qquad \tilde{P}_2 = (0,0,-3.40+\delta w_2^{(2)}),\\
&\tilde{P}_3 = (0,-2.94+\delta y_3^{(2)}, -1.70+\delta w_3^{(2)}),\\
&\tilde{P}_5 = (-0.651+\delta x_5^{(2)}, -0.981+\delta y_5^{(2)}, -1.70+\delta w_5^{(2)}).
\end{aligned} \tag{4.13}$$

In the notations $\delta x_i^{(a)}, \delta y_i^{(a)}, \delta w_i^{(a)}$, $a = 1,\ldots,5$ labels the tetrahedron, and $i = 1,\ldots,5$ labels the variables associated to the vertex $\tilde{P}_i$. There are 30 variables $\delta x_i^{(a)}, \delta y_i^{(a)}, \delta w_i^{(a)}$ in total. We keep the face areas unchanged. Then in each tetrahedron, Heron's formula gives four constraint equations, each corresponding to a face area. For example, in the tetrahedron $e_2 = \{1,2,3,5\}$, the equations are

$$\begin{cases}
A_{123}(\delta w_2^{(2)}, \delta y_3^{(2)}, \delta w_3^{(2)}) = 5\\
A_{125}(\delta w_2^{(2)}, \delta x_5^{(2)}, \delta y_5^{(2)}, \delta w_5^{(2)}) = 2\\
A_{135}(\delta y_3^{(2)}, \delta w_3^{(2)}, \delta x_5^{(2)}, \delta y_5^{(2)}, \delta w_5^{(2)}) = 2\\
A_{235}(\delta w_2^{(2)}, \delta y_3^{(2)}, \delta w_3^{(2)}, \delta x_5^{(2)}, \delta y_5^{(2)}, \delta w_5^{(2)}) = 2.
\end{cases} \tag{4.14}$$

At least in a neighborhood of the deformation, $\delta w_2^{(2)}, \delta y_3^{(2)}, \delta w_3^{(2)}, \delta x_5^{(2)}$ can be solved in terms of $\delta y_5^{(2)}, \delta w_5^{(2)}$ from (4.14). The shape of the tetrahedron is parametrized by two variables $\delta y_5^{(2)}, \delta w_5^{(2)}$. This way of parametrization is convenient in our computation. However, it is different from the known strategy, such as the Kapovich-Millson phase space [46] or using dihedral angles [47]. For each tetrahedron, we adopt the same strategy. We have in total ten variables $\mathrm{B} \equiv (\delta y_4^{(1)}, \delta w_4^{(1)}, \delta y_5^{(2)}, \delta w_5^{(2)}, \delta y_5^{(3)}, \delta w_5^{(3)}, \delta y_5^{(4)}, \delta w_5^{(4)}, \delta w_5^{(5)}, \delta w_5^{(5)})$ to parametrize the deformation of five tetrahedra. The spinors ξ_{ef} of each face can be expressed in terms of B according to (4.12). At this point, the boundary data is $r(\mathrm{B}) = (j_f, \xi_{ef}(\mathrm{B}))$. We insert $r(\mathrm{B})$ into the action $S(r(\mathrm{B}), x)$ in (4.2), whose analytical extension is $\mathcal{S}(r(\mathrm{B}), z)$. Then, the complex critical equations are $F(\mathrm{B}, z) = \partial_z \mathcal{S}(r(\mathrm{B}), z) = 0$, from which we solve for the complex critical point $z(\mathrm{B})$.

The asymptotics of the four-simplex amplitude with the boundary data violating the shape-matching condition is given by (3.8). Here, the complex critical point $z(\mathrm{B})$ inserting into the analytic continued action gives $\mathcal{S}(r(\mathrm{B}), z(\mathrm{B}))$. In contrast to the Regge action obtained from spinfoam asymptotics in [8], $\mathcal{S}(r(\mathrm{B}), z(\mathrm{B}))$ is an action of the twisted geometry [48].[2] Indeed, $\mathcal{S}(r(\mathrm{B}), z(\mathrm{B}))$ depends on the degrees of freedom of semiclassical tetrahedra, which are not constrained by the shape-matching condition. These degrees of freedom are beyond the Regge geometry and belong to the twisted geometry of the boundary.

To solve the complex critical point, we can linearize (4.14) and obtain the linear solution $(\delta w_2^{(2)}, \delta y_3^{(2)}, \delta w_3^{(2)}, \delta x_5^{(2)})$ in

[2]The condition for shape matching differs from the shape matching condition discussed in [48]. In their work, Freidel *et al.* [48] introduced an additional angle variable as a degree of freedom in twisted geometry, which is canonically conjugate to the area variable. While these two conditions share an intuitive similarity, they are not precisely identical.

terms of $\delta y_5^{(2)}, \delta w_5^{(2)}$. We can also linearize the complex critical equation at $\mathrm{B} = (0, \ldots, 0)$, and then solve for the complex critical point $z = z^{(\mathrm{lin})}(\mathrm{B})$. The solution $z^{(\mathrm{lin})}(\mathrm{B})$ is a linear function of the perturbations B. The coefficients in the linear function can be computed numerically. Inserting this linear solution into the action, we obtain $\mathcal{S}(r(\mathrm{B}), z^{(\mathrm{lin})}(\mathrm{B}))$ as a function of B and expand it to the second order,

$$\mathcal{S}(r(\mathrm{B}), z^{(\mathrm{lin})}(\mathrm{B})) = \mathfrak{Q}_{ij}\mathrm{B}^i\mathrm{B}^j + \mathfrak{L}_j\mathrm{B}^j + \mathcal{S}_0, \qquad (4.15)$$

where the coefficients $\mathfrak{Q}_{ij}, \mathfrak{L}_j$ can be computed numerically. $\mathcal{S}_0$ is the spinfoam action evaluated at the real critical point with $\mathrm{B} = (0, \ldots, 0)$. In Fig. 3, we let $\mathrm{B} = (0, 0, 0, \delta w_5^{(2)}, 0, 0, 0, 0, 0, 0)$, the red curves in (a) and (b) are the real part and imaginary part of $\mathcal{S}(r(\mathrm{B}), z^{(\mathrm{lin})}(\mathrm{B}))$ with $\delta w_5^{(2)}$ varying from -1 to 1.

The linear solution may have a large error when components in B are large. We apply the Newton-Raphson method to numerically search for the solution, which is more accurate than the linear solution. To compare with the linear solution in Fig. 3, we still only focus on the deformation of $e_2 = \{1, 2, 3, 5\}$ and set $\delta y_5^{(2)} = 0$. We outline the procedure in the following.

For any given $\delta w_5^{(2)}$, we can numerically solve Eq. (4.14) for $(\delta w_2^{(a)}, \delta y_3^{(a)}, \delta w_3^{(a)}, \delta x_5^{(a)})$. There are multiple solutions. We select the solution that is within a neighborhood at (0, 0, 0, 0), by requiring $|\delta w_2^2 + \delta y_3^2 + \delta w_3^2 + \delta x_5^2| \leq 4|\delta w_5^2|$. The coordinates in (4.13) given by the solution result in the 3d face normal vectors $\vec{n}$ and spinors ξ, which are the boundary data r violating the shape-matching condition.

We apply the Newton-Raphson method to search for the complex critical point satisfying $\partial_z \mathcal{S} = 0$. An outline of the procedure in the Newton-Raphson method is given in Appendix B. In Fig. 3, the blue curves in (a) and (b) are the real part and imaginary part of the analytically continued action at the complex critical points. This numerical result (blue curves) and the result from the linear solution (red curves) are close when the deformation is small. However, the linear solution is less accurate when the deformation is large.

Figure 3 demonstrates the smooth interpolation between the oscillatory and exponential suppression behaviors mentioned at the beginning of this subsection. In addition to scaling large λ, we need to consider the smooth deformation B. For any given λ, there exists sufficiently small deformation B beyond the shape matching, such that $\mathrm{Re}(\mathcal{S})$ is small, and thus the amplitude is not suppressed.

V. REVISITING THE Δ_3 AMPLITUDE

In this section, we revisit briefly the existing result on the spinfoam amplitude on the Δ_3 complex, for the completeness and preparing the discussion of the double-Δ_3 complex in the next section. The Δ_3 complex contains a single internal face $F = 1$ but has no internal segment $M = 0$. There is an internal j_h that is an integrated variable in the amplitude $A(\Delta_3)$ in (2.16).

The Δ_3 complex and its dual cable diagram are represented in Fig. 4. All tetrahedra and triangles are spacelike. The Regge geometry on Δ_3 is completely fixed by the Regge boundary data $\{j_b, \xi_{eb}\}$ that is determined by the boundary segment lengths. In this section, we only focus on the Regge boundary data, in contrast to the discussion of four-simplex amplitude in the previous section. The generalization to non-Regge boundary data should be straightforward. In terms of the notation in Sec. III, we have $r = \{j_b, \xi_{eb}\}$ as the boundary data. $\mathring{r} = \{\mathring{j}_b, \mathring{\xi}_{eb}\}$ fixes the flat geometry $\mathbf{g}(\mathring{r})$ with deficit angle $\delta_h = 0$. $\mathring{x} = \{\mathring{j}_h, \mathring{g}_{ve}, \mathring{\mathbf{z}}_{vf}\}$ is the real critical point associated to $\mathring{r}$. The data $\mathring{r}$, $\mathbf{g}(\mathring{r})$, and $\mathring{x}$ are computed numerically in [12].

According to the general spinfoam amplitude (2.16) and the spinfoam action (2.17), the Δ_3 amplitude $A(\Delta_3)$ can be written as

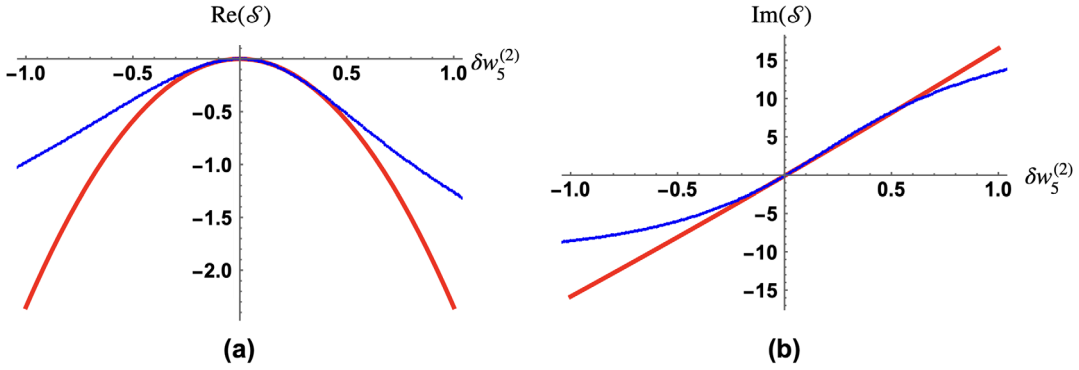

FIG. 3. In both panels, the blue curves are the numerical results with the Newton-Raphson method, and the red curves are the results from the linear solution. Panel (a) is the real part of the analytically continued action $\mathcal{S}$ at the complex critical points varying with $\delta w_5^{(2)}$. Panel (b) is the imaginary part of $\mathcal{S}$ at the complex critical points varying with $\delta w_5^{(2)}$. The range of $\delta w_5^{(2)}$ is $[-1, 1]$.

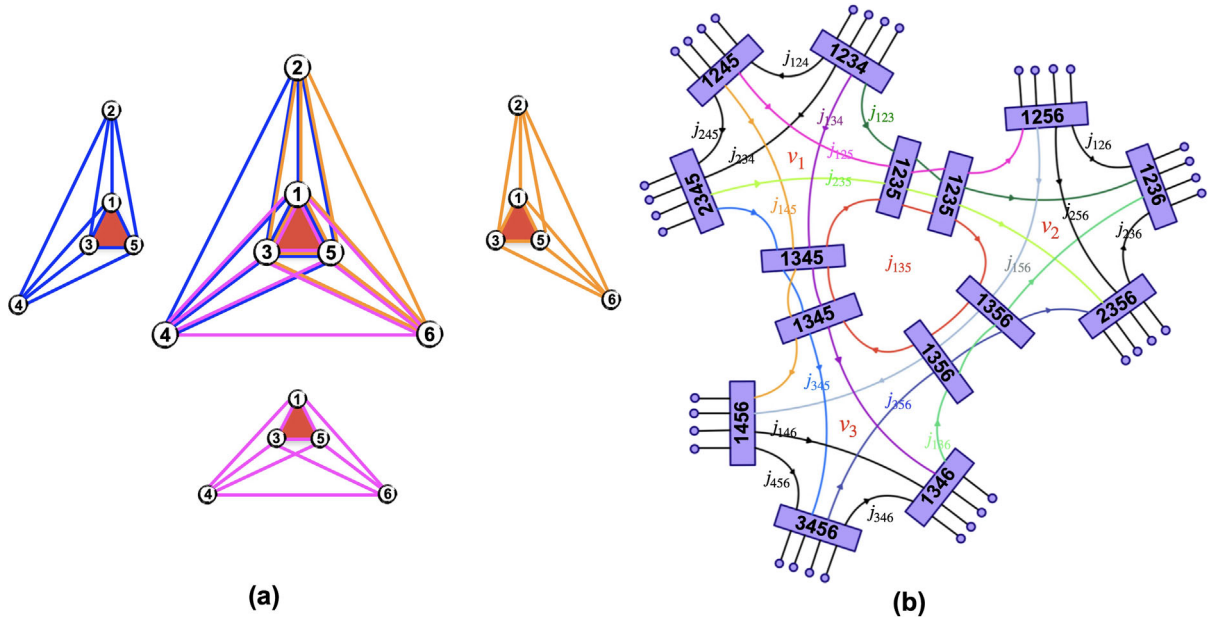

FIG. 4. Panel (a) illustrates the simplicial complex Δ_3 made by three four-simplices $\{v_1, v_2, v_3\}$ and 12 tetrahedra e_i sharing nineteen faces f_i. There are eighteen boundary faces and one internal face. Panel (b) is the dual cable diagram of the Δ_3 spinfoam amplitude: The boxes correspond to tetrahedra carrying $g_{ve} \in \mathrm{SL}(2,\mathbb{C})$. The strands stand for triangles carrying spins j_f. The strand with the same color belonging to a different dual vertex corresponds to the triangle shared by the different four-simplices. The circles as the endpoints of the strands carry boundary states $|j_b, \xi_{eb}\rangle$. The arrows represent orientations. This figure is adapted from [49].

$$A(\Delta_3) = \sum_{k_h \in \mathbb{Z}} 2\lambda \int \mathrm{d}j_h d_{\lambda j_h} \int [\mathrm{d}g\mathrm{d}\mathbf{z}] e^{\lambda S^{(k)}},$$
$$S^{(k)} = S + 4\pi i \sum_h j_h k_h. \tag{5.1}$$

For each k_h in (5.1), the real critical point $\{\overset{\circ}{j}_h, \overset{\circ}{g}_{ve}, \overset{\circ}{\mathbf{z}}_{vf}\}$ happens only when the boundary data satisfies the accidental flatness constraint (3.3).

Given the boundary data $\overset{\circ}{r}$ corresponding to $\delta_h = 0$, we consider its neighborhood U in the space of the nondegenerate Regge boundary data, such that any boundary data $r \in U$ satisfies $|\gamma\delta_h| < 4\pi$. For large λ, the sectors with $k_h \neq 0$ do not give dominant contribution to $A(\Delta_3)$ as far as $r \in U$. If we arbitrarily fix the boundary data $r \in U$ and scale λ large, the amplitude has two asymptotic behaviors analogous to the discussion at the beginning of Sec. IV B

(i) For the boundary data that corresponds to a flat Regge geometry, there is a real critical point, and the amplitude gives an oscillatory phase.
(ii) For the boundary data corresponding to a curved Regge geometry, there are no real critical points, and the amplitude is exponentially suppressed.

However, this way of presenting the asymptotic behavior leads to confusion about the flatness problem. From the discussion in Sec. III, it is clear that there is a smooth interpolation between the oscillatory phase and the exponential suppression behaviors, since the boundary data varies smoothly. The interpolation is obtained by applying the method of the complex critical point. The formal discussion of the complex critical point and the asymptotic behavior of this model have been given in [12]. Figure 5(a) plots $e^{\lambda \mathrm{Re}(\mathcal{S})}$ in the asymptotic formula (3.8) versus δ_h determined by the boundary data and demonstrates the smooth interpolation between the above two asymptotic behaviors. Letting the boundary data vary at the same time as scaling λ, we find the boundary data for the curved geometries with small nonzero δ_h for any λ, such that the amplitude $A(\Delta_3)$ is not suppressed, shown in Fig. 5(b). The range of δ_h for nonsuppressed $A(\Delta_3)$ is nonvanishing as far as λ is finite. The range of δ_h is enlarged when γ is small, shown in Fig. 5(c). δ_h that leads to non-suppressed $e^{\lambda \times \mathrm{Re}[\mathcal{S}(Z(r))]}$ satisfies the bound

$$|\gamma\delta_h| \lesssim \lambda^{-1/2}. \tag{5.2}$$

The above result provides evidence for the emergence of curved geometries from the spinfoam amplitude. The bound (5.2) is consistent with the earlier proposal [11] and the result in the effective spinfoam model [13,27,50]. So far, the bound (5.2) has only been confirmed in the regime of small or finite γ as we are going to see in Sec. VII, in the large-γ regime, geometries are violating the bound (5.2) but still giving a nonsuppressed contribution to the spinfoam amplitude.

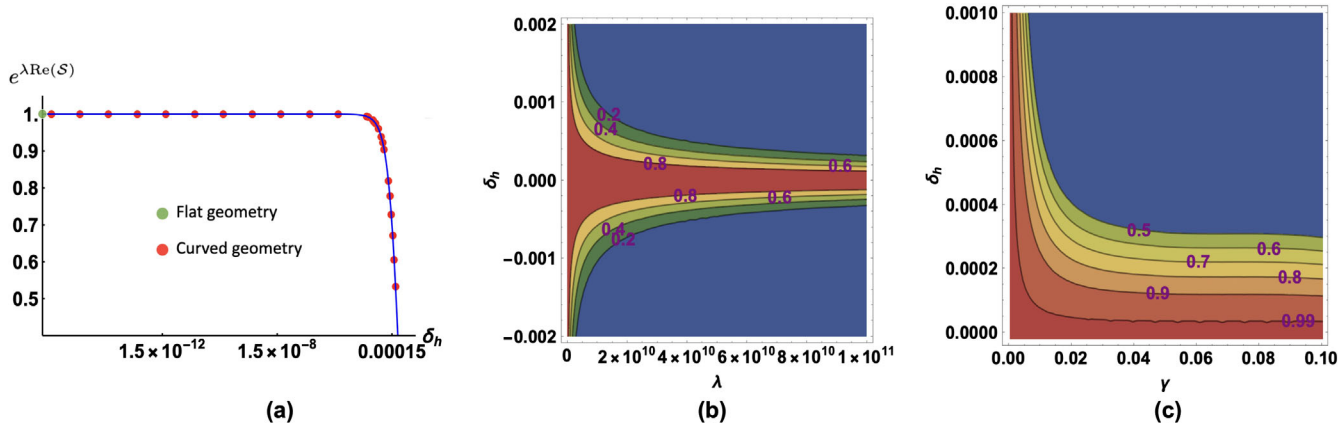

FIG. 5. Panel (a) plots $e^{\lambda \mathrm{Re}(\mathcal{S})}$ versus the deficit angle δ_h at $\lambda = 10^{11}$ and $\gamma = 0.1$ in $A(\Delta_3)$. The panels (b) and (c) are the contour plots of $e^{\lambda \mathrm{Re}(\mathcal{S})}$ as functions of (λ, δ_h) at $\gamma = 0.1$ and of (γ, δ_h) at $\lambda = 5 \times 10^{10}$ in $A(\Delta_3)$. They demonstrate the (nonblue) regime of curved geometries where the spinfoam amplitude is not suppressed. These figures first appeared in [12].

VI. DOUBLE-Δ_3 AMPLITUDE AND EFFECTIVE ACTION

A. Some setups

The Δ_3 complex does not have any internal segment, and the boundary data determines the Regge geometry completely. $A(\Delta_3)$ does not give the l_I-integral as in (3.10) by $M = 0$, so the effective dynamics of Regge geometry is trivial. In this section, we study the spinfoam amplitude on the "double-Δ_3" complex [see Fig. 6(a)], which is denoted by Δ_3^2. The double-Δ_3 complex contains a single internal segment, so $M = 1$, and thus $A(\Delta_3^2)$ gives (3.10) as a one-dimensional integral. So the double-Δ_3 complex admits nontrivial effective dynamics of the Regge geometry. Note that the same complex is also considered in the context of the effective spinfoam model [50].

The double-Δ_3 complex glues a pair of Δ_3 complex around the internal segment (1, 2). The complex has seven points $P_1 \ldots, P_7$. The four-simplices are given by

$$\{v_1, \ldots, v_6\} = \{(1,2,3,4,6), (1,2,3,5,6), (1,2,4,5,6), (1,2,3,4,7), (1,2,3,5,7), (1,2,4,5,7)\}.$$

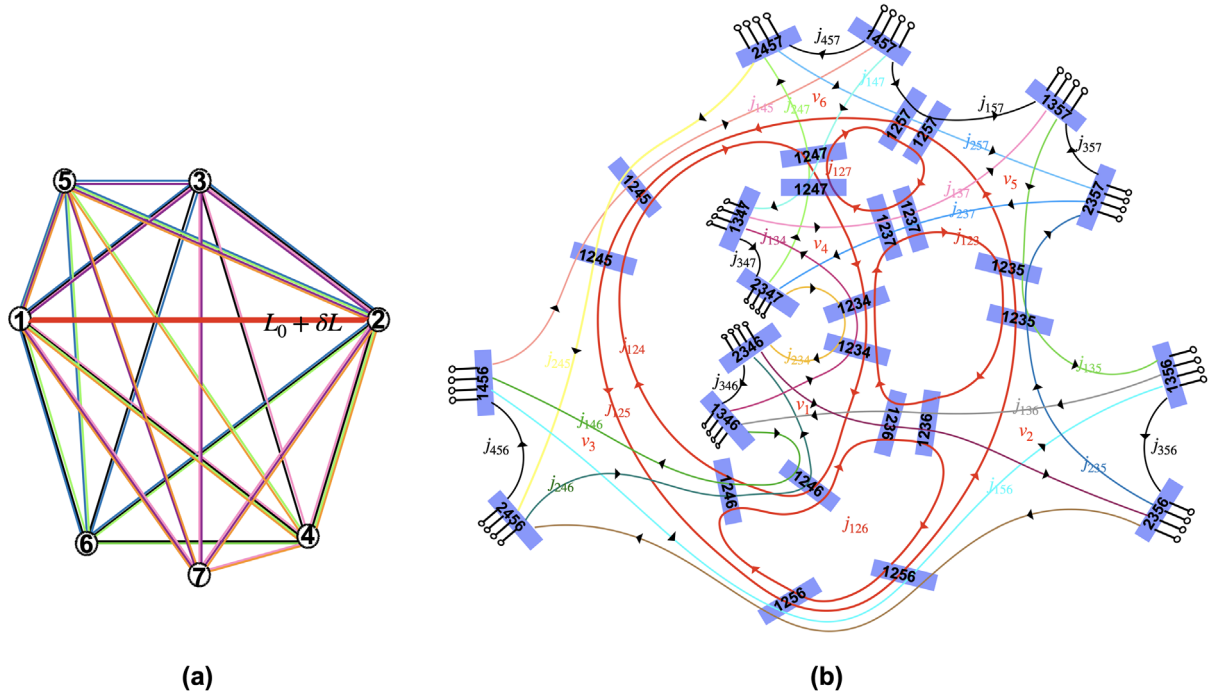

FIG. 6. A complex made of six simplices sharing the bulk edge (1, 2) with length l_{12} (the red line in panel (a)). In panel (a), the boundary edges are colored black, blue, violet, and cyan. The bulk edge is colored red. Panel (b) is the dual complex of the triangulation. The internal faces carrying j_{123}, j_{124}, j_{125}, j_{126}, j_{127}, are bounded by red loops, and other faces are boundary faces.

The tetrahedra are labeled by $\{e_1,\ldots,e_{21}\}$.[3] There are twelve boundary tetrahedra and nine internal tetrahedra among them. $j_h=\{j_{123},j_{124},j_{125},j_{126},j_{127}\}$ are carried by five internal triangles, whose dual faces are bounded by red loops shown in the dual diagram Fig. 6(b). Since there is only one internal segment (1, 2) and all other segments are on the boundary, the boundary data and the length l_{12} of the internal segment determine the Regge geometry $\mathbf{g}(r)$ on Δ_3^2. Following the procedure described in (3.5) and (3.6), we pick up the internal spin j_{123} and express the spinfoam amplitude as

$$\begin{aligned} A(\Delta_3^2)&=\int \mathrm{d}j_{123}\mathcal{Z}(j_{123};j_b,\xi_{eb}),\\ \mathcal{Z}(j_{123};j_b,\xi_{eb})&=\sum_{\{k_h\}}\int\prod_{\bar{h}=1}^{4}\mathrm{d}j_{\bar{h}}\prod_{h=1}^{5}2\lambda\tau_{[-\epsilon,\lambda j^{\max}+\epsilon]}(\lambda j_h)\\ &\quad\times\int\mathrm{d}\mu(g,\mathbf{z})e^{\lambda S^{(k)}}, \end{aligned}\tag{6.1}$$

where $j_{\bar{h}}=\{j_{124},j_{125},j_{126},j_{127}\}$. The external data of $\mathcal{Z}$ is $r_l=\{j_{123}(l_{12});j_b,\xi_{eb}\}$ including both the boundary data and $j_{123}(l_{12})$. Identifying γj_f to be the area of f (in Planck units), the Heron's formula

$$\gamma j_{123}(l_{12})=\frac{1}{4}\sqrt{4l_{12}^2l_{13}^2-(l_{12}^2+l_{13}^2-l_{23}^2)^2}\tag{6.2}$$

relates j_{123} to the internal segment length l_{12} and boundary segment lengths l_{13}, l_{23}. We consider the Regge boundary data that determines all the boundary segment lengths. We can always make a local change of the real variable $j_{123}\to l_{12}$ within a neighborhood K of a given Regge geometry, where the correspondence $j_{123}\leftrightarrow l_{12}$ is one-to-one.

In the following discussion, we only focus on the case with $k_h=0$. The Regge geometries under consideration are of small deficit angles. The following describes the procedure to compute the complex critical points $Z(r_l)$ of $\mathcal{Z}$.

We embed the double-Δ_3 complex in $(\mathbb{R}^4,\eta_{IJ})$ and determines a flat Regge geometry with all tetrahedra spacelike. We assign the following coordinates to the points,

$$\begin{aligned} &P_1=(0,0,0,0),\quad P_2=(-0.0680,-0.220,-0.532,-1.33),\\ &P_3=(0,0,0,-3.40),\\ &P_4=(-0.240,-0.694,-0.981,-1.70),\\ &P_5=(0,0,-2.94,-1.70),\quad P_6=(0,-2.77,-0.981,-1.70),\\ &P_7=(-2.47,-3.89,-1.36,-1.91). \end{aligned}$$

From the coordinates, we can compute the length of the segments of the triangulation by using

$$l_{ij}=\sqrt{\eta_{IJ}(P_i-P_j)^I(P_i-P_j)^J}.\tag{6.3}$$

with $\eta_{IJ}=\mathrm{Diag}(\{-1,1,1,1\})$ the Minkowski metric. The segment lengths are shown in Table I. The triangles within a four-simplex are classified into two categories [8]. The triangle corresponds to the thin wedge if the inner product between the timelike normals of the two adjacent tetrahedra is positive, otherwise the triangle corresponds to the thick wedge. The dihedral angle θ_{v,e_i,e_j} are given by

$$\begin{aligned} &\text{thin wedge: } N_{ve_i}\cdot N_{ve_j}=\cosh\theta_{v,e_i,e_j},\\ &\text{thick wedge: } N_{ve_i}\cdot N_{ve_j}=-\cosh\theta_{v,e_i,e_j}, \end{aligned}\tag{6.4}$$

where the inner product is the Minkowski inner product defined by η. Then we check the deficit angles δ_{h_i} associated to the shared triangles h_i

$$\begin{aligned} 0=\delta_{h_1}&=\theta_{v_1,e_1,e_2}+\theta_{v_2,e_2,e_6}+\theta_{v_4,e_1,e_{13}}+\theta_{v_5,e_6,e_{13}}\\ &\approx 0.514+0.464-0.575-0.404,\\ 0=\delta_{h_2}&=\theta_{v_1,e_1,e_3}+\theta_{v_3,e_3,e_{10}}+\theta_{v_4,e_1,e_{15}}+\theta_{v_6,e_{10},e_{15}}\\ &\approx 1.08-1.02-1.30+1.24,\\ 0=\delta_{h_3}&=\theta_{v_2,e_6,e_7}+\theta_{v_3,e_7,e_{10}}+\theta_{v_5,e_6,e_{17}}+\theta_{v_6,e_{10},e_{17}}\\ &\approx -0.360-0.481+0.414+0.426,\\ 0=\delta_{h_4}&=\theta_{v_1,e_2,e_3}+\theta_{v_2,e_2,e_7}+\theta_{v_3,e_7,e_{10}}\\ &\approx -0.723-0.208+0.931,\\ 0=\delta_{h_5}&=\theta_{v_4,e_1,e_{15}}+\theta_{v_5,e_{13},e_{17}}+\theta_{v_6,e_{15},e_{17}}\\ &\approx -0.903+1.20-0.301, \end{aligned}\tag{6.5}$$

which implies the Regge geometry is flat. The data of the flat geometry determines the external data $\mathring{r}_l$ for the partial amplitude $\mathcal{Z}$, which has the real critical points $(\mathring{j}_{\bar{h}},\mathring{g}_{ve},\mathring{\mathbf{z}}_{vf})$ corresponding to this flat Regge geometry and endowing the consistent four-orientations to all four-simplices. The boundary data of the flat geometry and the real critical point can be found in Appendix C 1, and Mathematica code can be found in [51,52]. In this case, given the boundary data, the flat Regge geometry is the solution of the classical Regge equation of motion, and it is also the solution

[3]The tetrahedra are $\{e_1,\ldots,e_{21}\}=\{\{1,2,3,4\},\{1,2,3,6\},\{1,2,4,6\},\{1,3,4,6\},\{2,3,4,6\},\{1,2,3,5\},\{1,2,5,6\},\{1,3,5,6\},\{2,3,5,6\},\{1,2,4,5\},\{1,4,5,6\},\{2,4,5,6\},\{1,2,3,7\},\{1,2,4,7\},\{1,3,4,7\},\{2,3,4,7\},\{1,2,5,7\},\{1,3,5,7\},\{2,3,5,7\},\{1,4,5,7\},\{2,4,5,7\}\}$.

$(\mathring{j}_{\bar{h}}, \mathring{g}_{ve}, \mathring{\mathbf{z}}_{vf})$ to the critical equations from the spinfoam amplitude.

We are going to compare the classical Regge dynamics and the spinfoam effective dynamics for curved geometries. This comparison is based on the numerical computations. In concrete, we deform the boundary segment length $l_{35} \to l_{35} + 10^{-3}$ but keep the other boundary segment lengths unchanged. The boundary data does not admit any flat geometry on Δ_3^2 [see Fig. 7(b)].[4] With this deformation, a classical Regge solution (i.e., the solution to the classical Regge equation $\delta S_{\text{Regge}} = 0$) gives the deficit angles

$$\delta_{h_1} = 0.0118, \quad \delta_{h_2} = 0.0661, \quad \delta_{h_3} = -0.0215, \quad \delta_{h_4} = -0.0236, \quad \delta_{h_5} = -0.0252, \tag{6.6}$$

which implies that the classical Regge dynamics gives curved geometry. We fix the boundary data and vary the internal segment length $l_{12} = L_0 + \delta L$ where $L_0 = 1.45$ is the length l_{12} in the flat geometry. The change of l_{12} is denoted by δL with $\delta L \in [-0.0129, 0.00251]$.[5] The classical Regge action S_{Regge} as a function of δL is plotted in Fig. 7(a). The above solution leading to (6.6) is close to the origin $\delta L = 0$ and is denoted by $\delta L_c^{\text{Regge}}$. There exists another Regge solution in $\delta L < 0$ and far from $\delta L = 0$ as shown in Fig. 7(a). We denote this solution by $\delta \tilde{L}_c^{\text{Regge}}$.

Likely, the solution $\delta \tilde{L}_c^{\text{Regge}}$ is a discretization artifact because when smoothly deforming the boundary data l_{35} back to the one for the flat geometry, $\delta L_c^{\text{Regge}}$ reduces back to the flat solution. In contrast, $\delta \tilde{L}_c^{\text{Regge}}$ still reduces to a curved Regge geometry. Some boundary data also exist such that the second solution $\delta \tilde{L}_c^{\text{Regge}}$ disappears. Nevertheless, we will take into account both solutions $\delta L_c^{\text{Regge}}$ and $\delta \tilde{L}_c^{\text{Regge}}$ in discussing the effective dynamics in Sec. VII.

The boundary data (j_b, ξ_{ef}) and the corresponding pseudocritical points $(j_{\bar{h}}^0, g_{ve}^0, \mathbf{z}_{vf}^0)$ for the curved geometry with the boundary segment length $l_{35} \to l_{35} + 10^{-3}$ and the internal edge $l_{12} = L_0 + \delta L_c^{\text{Regge}}$ are listed in Appendix C 2.

Notice that the geometrical areas in the boundary data relate to j_b by $\mathfrak{a}_b = \gamma j_b$, and the area $\mathfrak{a}_b$ relates to the lengths l_{ij} by Heron's formula. The following discussion involves fixing the geometrical area $\mathfrak{a}_b$ and performing computations at different Barbero-Immirzi parameter γ, so this leads to different j_b at different γ. Fixing the geometrical area instead of fixing j_b is useful when we compare with the Regge action S_{Regge}, since S_{Regge} only depends on the geometrical boundary data.

B. Numerical computing the effective action

Given the boundary condition (j_b, ξ_{eb}) corresponds to the above Regge boundary data with the deformed l_{35}, and given any l_{12} and $j_{123}(l_{12})$ taking value inside a neighborhood of the value for the flat geometry, we find the pseudocritical point $(j_{\bar{h}}^0, g_{ve}^0, \mathbf{z}_{vf}^0)$ close to the real critical point inside the real integration domain. The pseudocritical point only satisfies $\text{Re}(S) = \partial_{g_{ve}} S = \partial_{\mathbf{z}_{vf}} S = 0$ but does not necessarily satisfy $\partial_{j_{\bar{h}}} S = 0$. The pseudocritical point $(j_{\bar{h}}^0, g_{ve}^0, \mathbf{z}_{vf}^0)$ is the critical point of the spinfoam amplitude with fixed j_h, j_b [9], and endows the Regge geometry $\mathbf{g}(r)$ and consistent four-simplex orientations to Δ_3^2 complex.[6] It reduces to the real critical point $(\mathring{j}_{\bar{h}}, \mathring{g}_{ve}, \mathring{\mathbf{z}}_{vf})$ when $r_l = \mathring{r}_l$ corresponds to the flat geometry on Δ_3^2. As the deformation of segment length l_{35} is small, this curved geometry is close to the flat geometry, so $(j_{\bar{h}}^0, g_{ve}^0, \mathbf{z}_{vf}^0)$ is close to $(\mathring{j}_{\bar{h}}, \mathring{g}_{ve}, \mathring{\mathbf{z}}_{vf})$ in the integration domain. The data for the pseudocritical point is listed in Appendix C 2.

In this computation, we still adopt the similar parametrizations of variables as in (4.5)–(4.7), but with the pseudocritical points as the origin. The parametrizations of the group element $g_{v_1e_2}, g_{v_2e_7}$, $g_{v_3e_3}$, $g_{v_4e_{13}}, g_{v_5e_{17}}$, $g_{v_6e_{15}}$, $g_{v_1e_1}, g_{v_2e_6}$, and $g_{v_3e_{10}}$ are upper-triangular matrices due to the SU(2) gauge fixing at nine internal tetrahedra

$$g_{ve} = g_{ve}^0 \begin{pmatrix} 1 + \frac{x_{ve}^1}{\sqrt{2}} & \frac{x_{ve}^2 + i y_{ve}^2}{\sqrt{2}} \\ 0 & * \end{pmatrix}, \tag{6.7}$$

where the entry $*$ is determined by $\det(g_{ve}) = 1$. The internal spin $j_{\bar{h}}$ is parametrized as

$$j_{\bar{h}} = j_{\bar{h}}^0 + \mathrm{j}_{\bar{h}}, \mathrm{j}_{\bar{h}} \in \mathbb{R}. \tag{6.8}$$

As a result, for $k_h = 0$, the spinfoam amplitude $A(\Delta_3^2)$ and $\mathcal{Z}(j_{123})$ in (6.1) can be written in the form of

$$A(\Delta_3^2) = \int \mathrm{d}l_{12} \left| \frac{\partial j_{123}}{\partial l_{12}} \right| \mathcal{Z}(j_{123}(l_{12}); j_b, \xi_{eb}),$$
$$\mathcal{Z}(j_{123}(l_{12}); j_b, \xi_{eb}) \sim \int \mathrm{d}^{241} x \mu(x) e^{\lambda S(r_l, x)},$$
$$r_l = (j_{123}(l_{12}), j_b, \xi_{eb}), \tag{6.9}$$

[4] If the boundary data admitted a flat Regge geometry on the complex, the flat geometry would be a solution to the Regge equation. However, the solution of the Regge equation is a curved geometry with the given boundary data, contradicting the assumption of admitting the flat geometry.

[5] The range used here is restricted by the existence of curved Regge geometry with all tetrahedra spacelike.

[6] Since the correspondence between j_{123} and l_{12} is not one-to-one globally, it might be possible to have multiple pseudocritical points corresponding to different Regge geometries with the same value of j_{123}. However, in our numerical analysis, the other l_{12} from the same j_{123} does not satisfy the triangle inequality. Therefore all pseudocritical points correspond to the same Regge geometry but with different four-simplex orientations, although we only focus on a fixed orientation.

where $x \equiv (x^1_{ve}, y^1_{ve}, x^2_{ve}, y^2_{ve}, x^3_{ve}, y^3_{ve}, x_{vf}, y_{vf}, \mathrm{j}_{\bar{h}})$. The parametrizations of (l_{12}, x) define the coordinate chart covering the neighborhood K enclosing $\tilde{x}_0 = (j_{123}, x_0) = (j^0_h, g^0_{ve}, \mathbf{z}^0_{vf})$, and $\mathring{\tilde{x}} = (\mathring{j}_{123}, \mathring{x}) = (\mathring{j}_h, \mathring{g}_{ve}, \mathring{\mathbf{z}}_{vf})$. This neighborhood is large enough since the parametrizations are valid generically. The pseudocritical point is $x_0 = (0, 0, \ldots, 0)$, which contains 241 zero components. Here we use "$\sim$" instead of "$=$" because (1) we only consider $k_h = 0$ but ignore other k_h terms,[7] (2) we only focus on the contribution from the neighborhood K enclosing a single pseudocritical point.[8] In our discussion, we only consider the effective dynamics within a sector of Regge geometries with the fixed 4D orientation.

We compute the complex critical point of $\mathcal{Z}$ for any given external data r_l. Here, both $S(r, x)$ and $\mu(x)$ are analytic in the neighborhood K of x_0. $S(r, x)$ can be analytically continued to a holomorphic function $\mathcal{S}(r_l, z)$, and $z \in \mathbb{C}^{241}$ is in a complex neighborhood of x_0. The analytic continuation is obtained by simply extending $x \in \mathbb{R}^{241}$ to $z \in \mathbb{C}^{241}$. The formal discussion of the analytic continuation of the spinfoam action is given in [14]. We fix the boundary data to be the one resulting in (6.6) and vary the length $l_{12} = L_0 + \delta L$, where $L_0 = 1.45$ (the value of l_{12} in Table I) and the change of l_{12}, $\delta L \in [-0.0129, 0.00251]$. For any given δL, combining the boundary data, we repeat the steps above (from the beginning of this subsection) to reconstruct the Regge geometry and the corresponding pseudocritical point. Taking the pseudocritical point as the starting point, we apply the Newton-Raphson method by repeating the steps in (B2)–(B8) to numerically compute the complex critical point $Z(r_l)$ for a sequence of δL. By evaluating $\mathcal{S}$ at the complex critical point and apply the asymptotic formula (3.8), we obtain the following asymptotic behavior of $\mathcal{Z}$ and $A(\Delta^2_3)$ for the dominant contribution from the integral on K

$$\mathcal{Z}(j_{123}(l_{12}); j_b, \xi_{eb}) \sim \left(\frac{1}{\lambda}\right)^{\frac{241}{2}} \mathcal{N}_l e^{\lambda \mathcal{S}(r_l, Z(r_l))}[1 + O(1/\lambda)],$$
$$A(\Delta^2_3) \sim \left(\frac{1}{\lambda}\right)^{\frac{241}{2}} \int \mathrm{d}l_{12} \left|\frac{\partial j_{123}}{\partial l_{12}}\right| \mathcal{N}_l e^{\lambda \mathcal{S}(r_l, Z(r_l))}[1 + O(1/\lambda)], \tag{6.10}$$

where $\mathcal{N}_l = \mu(Z(r_l)) \det(-\partial^2_{z,z} \mathcal{S}(r_l, Z(r_l))/2\pi)^{-1/2}$. Effectively, $A(\Delta^2_3)$ gives a path integral of Regge geometry on Δ^2_3. $\mathcal{S}(r_l, Z(r_l))$ is the effective action for the Regge geometry in the large-λ regime of the spinfoam amplitude.

[7]The integrals in the neighborhood K with $k_h \neq 0$ give exponentially suppressed contributions.

[8]there may exist other pseudocritical points outside K in $\mathcal{Z}$, e.g., the ones corresponding to different orientations of four-simplices. But our discuss only focuses on the critical points inside K.

TABLE I. Each cell of the table is the segment length for vertices P_i and P_j.

j	1	2	3	4	5	6	7
l_{ij}							
i							
1		1.45	3.40	2.07	3.40	3.40	3.81
2	1.45		2.14	0.729	2.45	2.62	2.96
3	3.40	2.14		2.07	3.40	3.40	3.62
4	2.07	0.729	2.07		2.07	2.07	2.34
5	3.40	2.45	3.40	2.07		3.40	3.41
6	3.40	2.62	3.40	2.07	3.40		
7	3.81	2.96	3.62	2.34	3.41		

The stationary phase approximation of the l_{12}-integral in (6.10) relates to the variation of $\mathcal{S}(r_l, Z(r_l))$ with respect to l_{12}. The effective equation of motion

$$\partial_{l_{12}} \mathcal{S}(r_l, Z(r_l)) = 0 \tag{6.11}$$

determines the effective dynamics of Regge geometry.

C. Comparing to Regge action

It is interesting to compare the effective action $\mathcal{S}(r_l, Z(r_l))$ to the classical Regge action S_{Regge} since both actions define the dynamics of Regge geometry. The definition of Regge action $S_{\mathrm{Regge}}(l_{12})$ is reviewed in Appendix D. In order to compare, we compute and plot the real and imaginary parts $\mathcal{S}_R$ and $\mathcal{S}_I$ of $\mathcal{S}(r_l, Z(r_l))$ respectively,

$$\mathcal{S}(r_l, Z(r_l)) = \mathcal{S}_R(\gamma, \delta L) + \mathrm{i}\mathcal{S}_I(\gamma, \delta L), \tag{6.12}$$

We view both $\mathcal{S}_R$ and $\mathcal{S}_I$ as functions of two variables γ and δL, and we compute the numerical values of $\mathcal{S}_R$ and $\mathcal{S}_I$ with samples of $\gamma \in [10^{-9}, 10^6]$ and $\delta L \in [-0.0129, 0.00251]$.

It is known that the spinfoam action contains an overall phase, which needs to be subtracted to compare to the Regge action. We denote the overall phase by $\phi(\gamma)$. This overall phase can be computed numerically by inserting the pseudocritical point $(j^0_{\bar{h}}, g^0_{ve}, \mathbf{z}^0_{vf})$ in the spinfoam action S and subtracting the Regge action at the corresponding geometry. Generally, we have

$$\phi(\gamma) = \alpha/\gamma, \tag{6.13}$$

where the coefficient α depends on the boundary data. In terms of the spinfoam variables, the overall phase comes from the γ-independent terms in S and is linear to the boundary spins $\phi \sim j_b$, but here we fix the boundary area and let γ vary, then $\phi \sim \mathfrak{a}_b/\gamma$. The numerical value of α is $\alpha = 0.003993$ resulting from our setup of the boundary data. In general, the overall phase in the spinfoam action

can be cancelled by the phase choice of boundary ξ_{eb}. To remove the overall phase from $\mathcal{S}_I$, we define $\mathcal{S}'_I$ by

$$\mathcal{S}_I(\gamma, \delta L) = -\mathcal{S}'_I(\gamma, \delta L) + \phi(\gamma). \tag{6.14}$$

$\mathcal{S}'_I$ as a function of δL is compared to the classical Regge action for different values of γ in Fig. 8. The minus sign in front of $\mathcal{S}'_I$ relates to the four-simplex orientation in the real and pseudocritical points. As indicated by Fig. 8, $\mathcal{S}'_I$ well-approximates the Regge action for small γ with negligible corrections. When increasing γ, $\mathcal{S}'_I$ gives nontrivial corrections to the Regge action.

For any given γ, the real part $\mathcal{S}_R$ is always negative, and $|\mathcal{S}_R|$ is larger for larger $|\delta L|$, so $e^{\lambda \mathcal{S}}$ is smaller for larger $|\delta L|$. However, if we fix δL and vary γ, $|\mathcal{S}_R|$ is smaller so $e^{\lambda \mathcal{S}}$ is less suppressed for any λ, when γ is smaller. In other words, the smaller γ opens a larger range of δL, in which $|\mathcal{S}_R|$ is small and $e^{\lambda \mathcal{S}}$ is not suppressed for a given λ. In this range of δL, the numerical result indicates that $\mathcal{S}(r_l, Z(r_l))$ well-approximates the Regge action. The similar situation has appeared in the Δ_3 amplitude, where the amplitude with smaller γ admits a wider range of curved geometries [see Fig. 5(c)].

VII. SOLUTIONS OF EFFECTIVE DYNAMICS ON DOUBLE-Δ_3

A. Spinfoam complex critical point and the Regge solution $\delta L_c^{\text{Regge}}$

The above discussion compares the effective action $\mathcal{S}(r_l, Z(r_l))$ to the classical Regge action. It is also interesting to compare the solution of the effective equation $\partial_{l_{12}} \mathcal{S}(r_l, Z(r_l)) = 0$ to the solution of the Regge equation. By the above computation, the real and imaginary parts of $\mathcal{S}(r_l, Z(r_l))$ are obtained as the numerical function. Numerically solving the effective equation involves finding the possible complex roots of numerical derivatives of the complex $\mathcal{S}(r_l, Z(r_l))$, which requires an estimation of $\mathcal{S}(r_l, Z(r_l))$ on the complex δL plane and may give a relatively large numerical error. In the following, we introduce an alternative strategy, which computes the solution of the effective equation more efficiently.

Instead of introducing the partial amplitude $\mathcal{Z}$, we consider the full spinfoam amplitude, which can be written as the following integral for the same contribution as in (6.10)

$$A(\Delta_3^2) \sim \int \mathrm{d}\delta L \mathrm{d}^{241} x \mu(\delta L, x) e^{\lambda \tilde{S}(r', \delta L, x)}. \tag{7.1}$$

Here the external parameter r' is just the boundary data $r' = (j_b, \xi_{eb})$. $\tilde{S}(r', \delta L, x)$ is the spinfoam action S with $j_{123} = j_{123}(l_{12})$ and $l_{12} = L_0 + \delta L$.

Recall that $\delta L_c^{\text{Regge}}$ is a solution of the classical Regge equation. The Regge geometry with $\delta L_c^{\text{Regge}}$ corresponds to a pseudocritical point of $\tilde{S}(r', \delta L, x)$. Both $\tilde{S}(r', \delta L, x)$ and $\mu(\delta L, x)$ are analytic in the neighborhood of this pseudocritical point. Therefore, $\tilde{S}(r', \delta L, x)$ and $\mu(\delta L, x)$ can be analytic continued to the holomorphic functions $\tilde{\mathcal{S}}(r', \delta \mathcal{L}, z)$ and $\mu(\delta \mathcal{L}, z)$, where $(\delta \mathcal{L}, z) \in \mathbb{C}^{242}$ is in a complex neighborhood of the pseudocritical point. We fix the boundary data r' to be the same as the one used in Fig. 7. Since r' is a small deformation from the boundary data of the flat geometry, the neighborhood covers the real critical point corresponding to the flat geometry and the boundary data before the deformation.

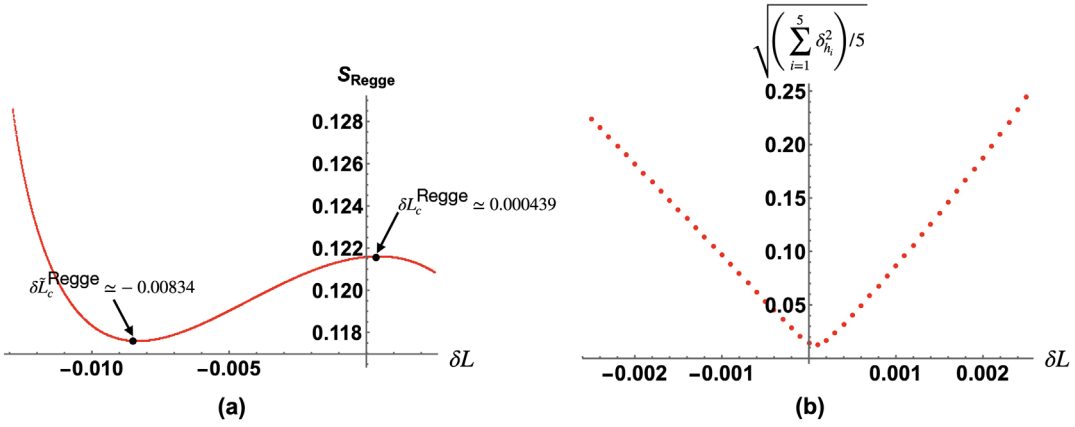

FIG. 7. Panel (a) is the Regge action varying with δL when we deform the boundary segment length $l_{35} \to l_{35} + 10^{-3}$ from the boundary data of the flat geometry. In this case, the Regge solutions are given by $\delta L_c^{\text{Regge}} \simeq 0.000439$ and $\delta \tilde{L}_c^{\text{Regge}} \simeq -0.00834$. Panel (b) is $\sqrt{(\sum_{i=1}^5 \delta_{h_i}^2)/5}$ versus δL with the deformed boundary data. All geometries in the range of δL are not flat. The minimum of $\sqrt{(\sum_{i=1}^5 \delta_{h_i}^2)/5}$ is 0.013.

For each γ, we would like to numerically compute the complex critical points $(\delta\mathcal{L}, z) = (\delta L_c^{\text{Spinfoam}}, \tilde{Z})(r')$ as the solution to the following equations:

$$\partial_z \tilde{\mathcal{S}}(r', \delta\mathcal{L}, z) = 0, \tag{7.2}$$

$$\partial_{\delta\mathcal{L}} \tilde{\mathcal{S}}(r', \delta\mathcal{L}, z) = 0. \tag{7.3}$$

Since we fix the boundary data r' and vary γ, the complex critical points give a continuous trajectory parametrized by γ in the complex space of $(\delta\mathcal{L}, z)$. In the numerical

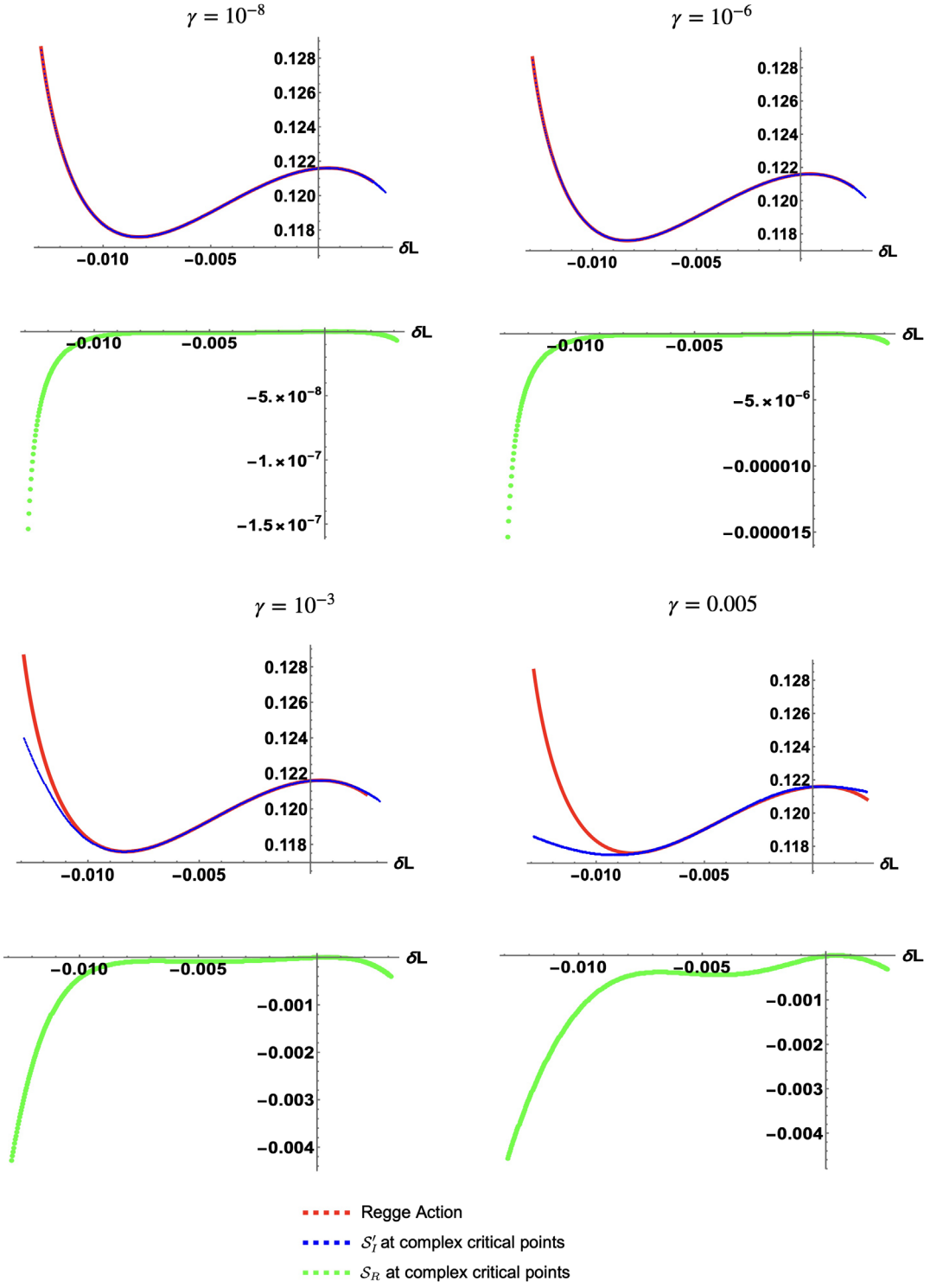

FIG. 8. The red curves plots the Regge action as a function of δL. In comparison to the Regge action, the blue curves plots $\mathcal{S}_I'$ of the analytic continued spinfoam action at complex critical points. The green curve plots the real part $\mathcal{S}_R$ of the analytic continued spinfoam action at complex critical points.

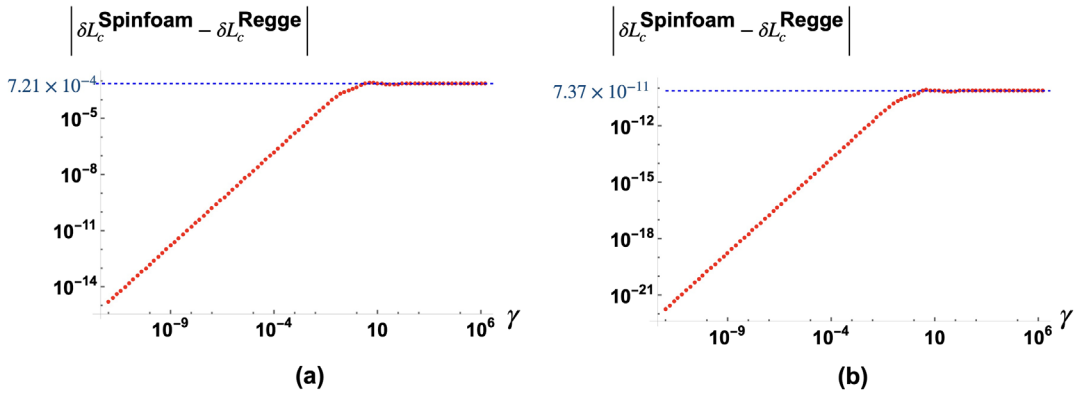

FIG. 9. Panels (a) and (b) are log-log plots of the distances (7.5) between the spinfoam and Regge solutions in a neighborhood of $\delta\mathcal{L} = 0$ as a function of γ. The boundary data has the boundary segment length l_{35} deformed from the flat geometry by $l_{35} \to l_{35} + 10^{-3}$ for (a) and $l_{35} \to l_{35} + 10^{-10}$ for (b).

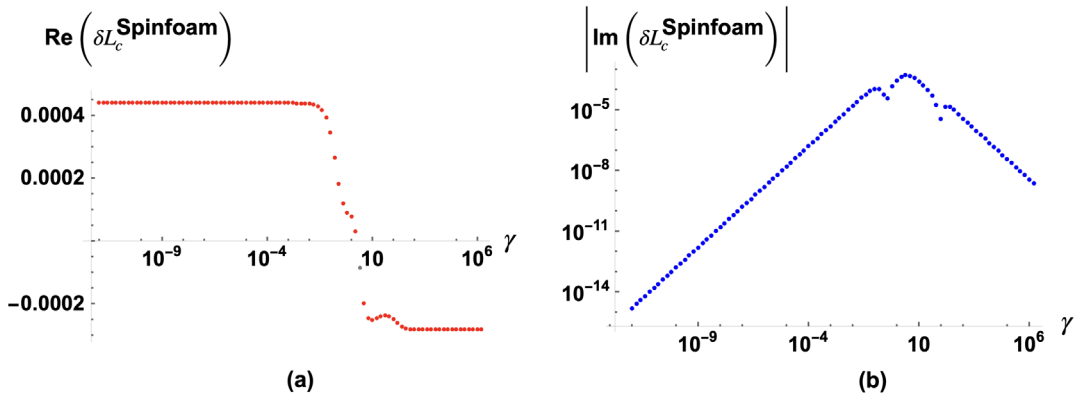

FIG. 10. Panels (a) show the real part of the spinfoam solution $\delta L_c^{\text{Spinfoam}}$ vs log-scaled γ value with the boundary data deformed from the flat geometry by $l_{35} \to l_{35} + 10^{-3}$. Panel (b) is the log-log plot of the absolute value of the imaginary parts of the spinfoam solution $\delta L_c^{\text{Spinfoam}}$ as a function of γ.

computation, we sample a sequence of $\gamma \in [10^{-9}, 10^{6}]$ and compute the complex critical point for each γ by the Newton-Raphson method, following the steps in (B2)–(B8). For any γ, the recursion of the Newton-Raphson method can be initialized at the pseudocritical point and give the convergent result within the desired tolerance. Moreover, all resulting complex critical points depend smoothly on the boundary data δl_{35} and reduces to the real critical point when $\delta l_{35} \to 0$ (see Fig. 13 for an example).

The solution $\delta\mathcal{L}$ from (7.2) and (7.3) is the same as the solution of $\partial_{\delta L}\mathcal{S}(r_l, Z(r_l)) = 0$. Indeed,

$$\begin{aligned} 0 &= \partial_{\delta L}\mathcal{S}(r_l, Z(r_l)) \\ &= \left.\frac{\partial\mathcal{S}(r_l, Z(r_l))}{\partial r_l}\right|_{Z(r_l)} \cdot \frac{\partial r_l}{\partial\delta L} + \left.\frac{\partial\mathcal{S}(r_l, Z(r_l))}{\partial Z(r_l)}\right|_{r_l} \cdot \frac{\partial Z(r_l)}{\partial\delta L} \\ &= \left.\frac{\partial\mathcal{S}(r_l, Z(r_l))}{\partial r_l}\right|_{Z(r_l)} \cdot \frac{\partial r_l}{\partial\delta L} = [\partial_{\delta L}\mathcal{S}(r_l, z)]_{z=Z(r_l)}, \end{aligned} \tag{7.4}$$

where we have used $\partial\mathcal{S}(r_l, Z(r_l))/\partial Z(r_l)|_{r_l} = 0$. $Z(r_l)$ depends on δL. $z = Z(r_l)$ is the solution of (7.2), when analytic continuing $\delta L \to \delta\mathcal{L}$. The result $[\partial_{\delta L}\mathcal{S}(r_l, z)]_{z=Z(r_l)} = 0$ from (7.4), followed by analytic continuing $\delta L \to \delta\mathcal{L}$, is equivalent to (7.3) with the solution of (7.2) inserted.

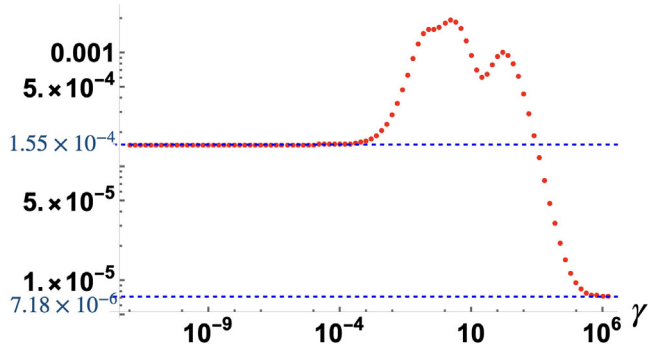

FIG. 11. The log-log plot of the average of the absolute value of the imaginary part of the complex critical point vs γ.

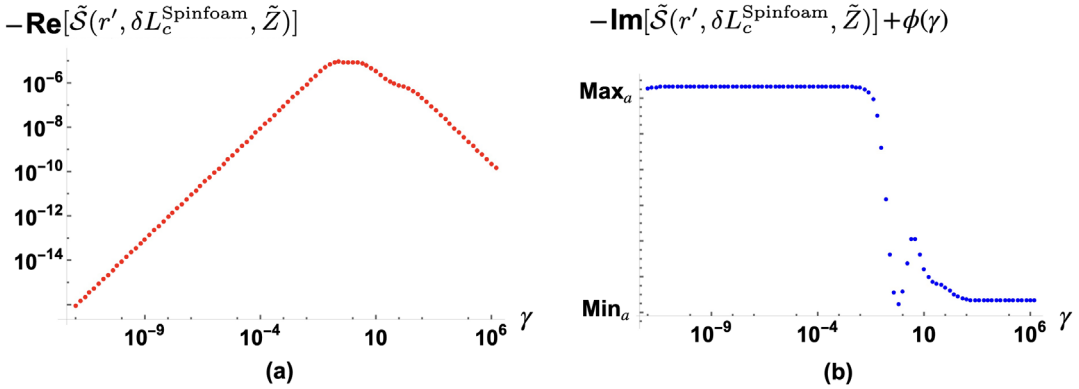

FIG. 12. Panels (a) are the log-log plot of the negative real parts of $\tilde{\mathcal{S}}(r', \delta\mathcal{L}, z)$ at the complex critical points $z = \tilde{Z}(r', \delta\mathcal{L})$ as a function of γ with the boundary data deformed from the flat geometry by $l_{35} \to l_{35} + 10^{-3}$. Panels (b) show the imaginary parts of $\tilde{\mathcal{S}}(r', \delta\mathcal{L}, z)$ at the complex critical points $z = \tilde{Z}(r', \delta\mathcal{L})$ vs log-scaled γ. We subtract the overall phase $\phi(\gamma)$ from $\text{Im}[\tilde{\mathcal{S}}(r', \delta L_c^{\text{Spinfoam}}, \tilde{Z})]$ and add a minus sign in plotting (b). In panel (b), the overall phase $\phi(\gamma) \simeq 0.003993\gamma^{-1}$, and the maximum and minimum of the plot range are $\text{Max}_a \simeq 0.121606$ and $\text{Min}_a \simeq 0.121596$.

The complex critical point gives $\delta\mathcal{L} \equiv \delta L_c^{\text{Spinfoam}}(\gamma)$ as a trajectory parametrized by γ in a complex neighborhood at $\delta\mathcal{L} = 0$, see Figs. 10(a) and 10(b). This solution is compared to the Regge solution $\delta L_c^{\text{Regge}} \simeq 0.000439$ (recall Fig. 7(a)). This solution $\delta L_c^{\text{Spinfoam}}(\gamma)$ is complex generically, although it is close to the real axis, especially for small γ. Figure 9(a) demonstrates the distance (in the complex plane) between the spinfoam solution $\delta L_c^{\text{Spinfoam}}(\gamma)$ and the classical Regge solution $\delta L_c^{\text{Regge}}$,

$$|\delta L_c^{\text{Spinfoam}}(\gamma) - \delta L_c^{\text{Regge}}|. \tag{7.5}$$

This distance is small in the small-γ regime. So the classical Regge dynamics is reproduced by the spinfoam effective dynamics for small γ. This result is consistent with comparing the actions in Fig. 8. This result is also consistent with some earlier arguments in [17–20] about the semiclassical approximation of spinfoams with small γ.

The distance (7.5) becomes larger when increasing γ. It indicates that the spinfoam amplitude with larger γ gives larger correction to the classical Regge solution. Therefore the effective theory in the large-γ regime has more significant difference from the Regge gravity. Furthermore, the distance (7.5) stabilizes in the large-γ regimes, as shown in Fig. 9(a). The distance value where it stablizes becomes smaller when the boundary data is closer to the one for the flat geometry, by comparing Figs. 9(a) and 9(b). The small- and large-γ regimes might be viewed as two phases of the spinfoam amplitude. The effective dynamics is closer to the Regge dynamics for small γ but more different from the Regge dynamics for large γ.

The critical point $(\delta L_c^{\text{Spinfoam}}, \tilde{Z})(r')$ is generally complex for every γ (see Fig. 11). Figures 12(a) and 12(b) plot the analytic continued action $\tilde{\mathcal{S}}(r', \delta\mathcal{L}, z)$ [with the overall phase $\phi(\gamma)$ removed] evaluated at the complex critical points for a large number of samples of γ. The real part $\text{Re}(\tilde{\mathcal{S}})$ is close to zero for both the small-γ and large-γ regimes, so $e^{\lambda\tilde{\mathcal{S}}}$ in the asymptotic formula (3.8) is not suppressed for large λ for both the small and large γ. The nonsuppressed $e^{\lambda\tilde{\mathcal{S}}}$ for small γ has been anticipated since it can be predicted by the bound (5.2). But the nonsuppressed $e^{\lambda\tilde{\mathcal{S}}}$ with large λ in the large-γ regime violates the bound (5.2). This result suggests that the bound (5.2) is not universal but only valid for the small or finite γ.

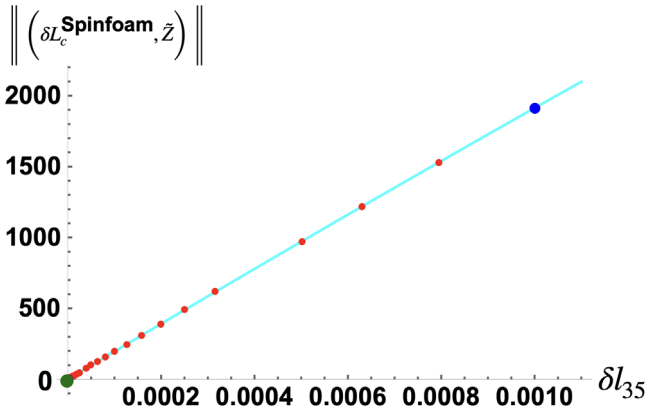

FIG. 13. The red points are the list-plot of the norm of the complex critical point $(\delta L_c^{\text{Spinfoam}}, \tilde{Z})$ vs the deformation of the boundary segment length δl_{35}. For any complex critical points $(\delta L_c^{\text{Spinfoam}}, \tilde{Z}) = (\delta L_c^{\text{Spinfoam}}, z_1, z_2, \ldots, z_{241})$, the norm is defined as $\|(\delta L_c^{\text{Spinfoam}}, \tilde{Z})\| = \sqrt{|\delta L_c^{\text{Spinfoam}}|^2 + |z_1|^2 + |z_2|^2 + \cdots + |z_{241}|^2}$. Here, the boundary segment length l_{35} is deformed from the flat geometry by $l_{35} \to l_{35} + \delta l_{35}$ at $\gamma = 10^{-6}$, $\delta l_{35} \in [0, 10^{-3}]$. The blue point is the complex critical point as $\delta l_{35} = 10^{-3}$, and the green point is the real critical point at the origin (0,0) corresponding to the flat geometry. The cyan curve represents the fitted function $\|(\delta L_c^{\text{Spinfoam}}, \tilde{Z})\| \simeq 1.97 \times 10^6 \delta l_{35} - 5.49 \times 10^7 (\delta l_{35})^2$.

Figure 9(b) plots $|\delta L_c^{\text{Spinfoam}} - \delta L_c^{\text{Regge}}|$ for the different boundary data, which deform the boundary data of the flat geometry by $l_{35} \to l_{35} + 10^{-10}$. This boundary data is closer to the boundary data for the flat geometry. The results are qualitatively similar to the results from the previous boundary data, although the maximum of $|\delta L_c^{\text{Spinfoam}} - \delta L_c^{\text{Regge}}|$ become smaller comparing to the results from the previous boundary data. Changing the boundary data seems not to shift the location in the γ-space, where the small-γ phase [where (7.5) is small] transits to the large-γ phase [where (7.5) is stabilizes], as suggested by comparing Figs. 9(a) and 9(b).

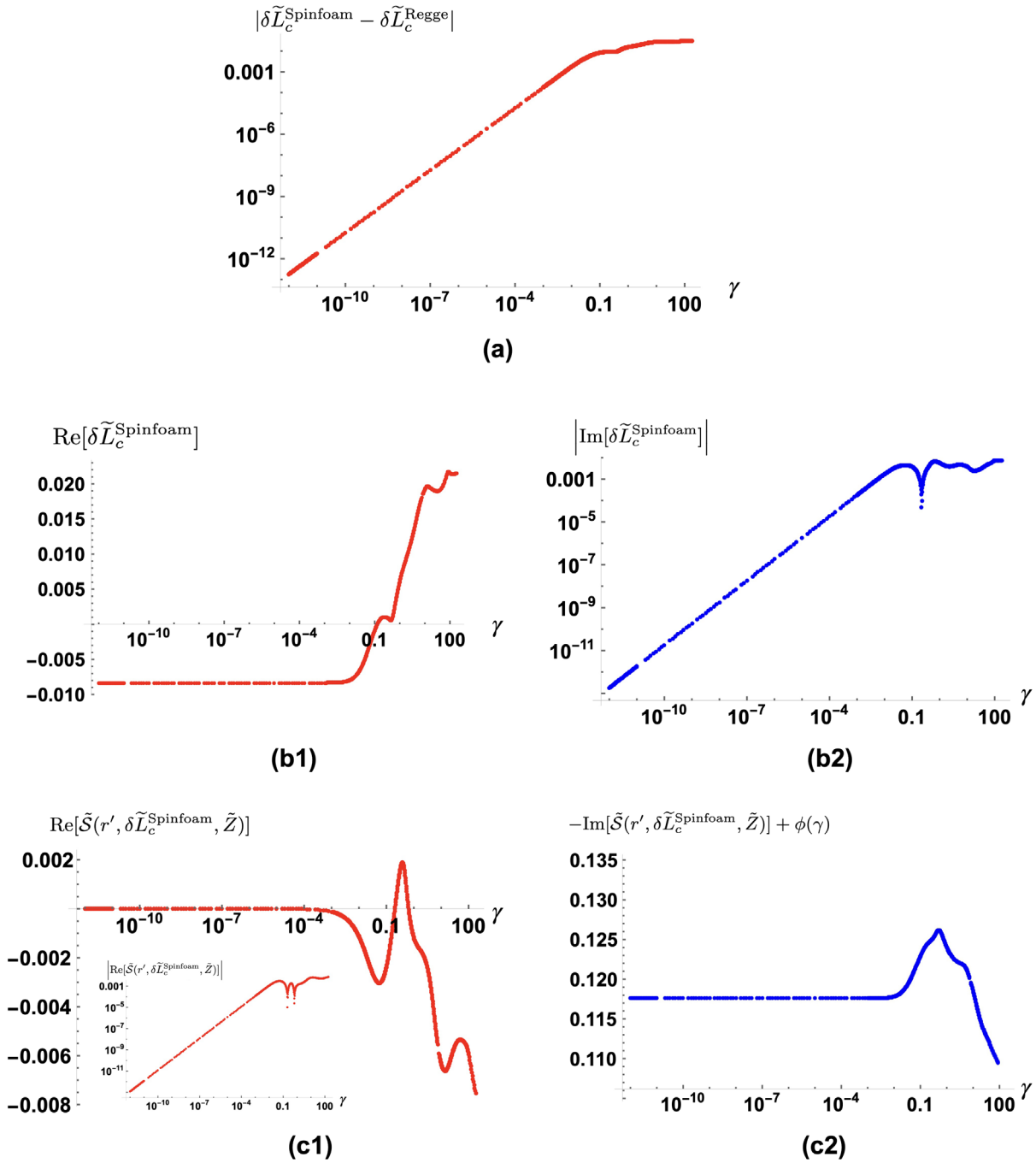

FIG. 14. Panel (a) is the log-log plot of the distance between the spinfoam solution and the Regge solution in a neighborhood of $\delta\tilde{L} = \delta\tilde{L}_c^{\text{Regge}}$ as a function of γ. Panel (b1) shows the real of the spinfoam solution $\delta\tilde{L}_c^{\text{Spinfoam}}$ vs γ. Panel (b2) is the log-log plot of the imaginary parts of the spinfoam solution $\delta\tilde{L}_c^{\text{Spinfoam}}$ vs γ. Panel (c1) is the real parts of $\tilde{\mathcal{S}}(r', \delta\tilde{\mathcal{L}}, z)$ at the complex critical points vs γ, and the small figure in (c1) is the log-log plot. Panel (c2) plots the imaginary parts of $\tilde{\mathcal{S}}(r', \delta\tilde{\mathcal{L}}, z)$ at the complex critical points vs γ.

B. Complex critical point and the other Regge solution $\delta\tilde{L}_c^{\text{Regge}}$

Recall from Fig. 7(a) that there is another classical Regge solution $\delta L = \delta\tilde{L}_c^{\text{Regge}}$ with the boundary condition under consideration. This solution corresponds to a different pseudocritical point, which we use as the starting point of initializing the recursion in the Newton-Raphson method. Following the same procedure discussed above, we obtain a new trajectory of complex critical points parameterized by γ. The complex critical point gives $\delta\mathcal{L} = \delta\tilde{L}_c^{\text{Spinfoam}}(\gamma)$, which is generically complex. Figure 14 plots the distance $|\delta\tilde{L}_c^{\text{Spinfoam}}(\gamma) - \delta\tilde{L}_c^{\text{Regge}}|$, the real and imaginary part of the $\delta\tilde{L}_c^{\text{Spinfoam}}(\gamma)$, and the real and imaginary part of the action $\tilde{\mathcal{S}}$ evaluated at the complex critical points. For small γ, $\delta\tilde{L}_c^{\text{Spinfoam}}(\gamma)$ is approximately real and close to the classical Regge solution $\delta\tilde{L}_c^{\text{Regge}}$. Increasing γ results in that $\delta\tilde{L}_c^{\text{Spinfoam}}(\gamma)$ makes larger corrections to $\delta\tilde{L}_c^{\text{Regge}}$.

Both the complex critical point here, denoted by $(\delta\tilde{L}_c^{\text{Spinfoam}}, \tilde{Z})(r')$, and $(\delta L_c^{\text{Spinfoam}}, \tilde{Z})(r')$ discussed in the last subsection give contributions to $A(\Delta_3^2)$. When we compare their contributions. $e^{\lambda\mathcal{S}}$ is suppressed faster at the critical point here than at the one in the last subsection (see Fig. 15) for fixed $\gamma < 0.1$. This relates to the fact that $\delta\tilde{L}_c^{\text{Regge}}$ gives larger deficit angles. Therefore the complex critical point here contributes to the amplitude much less than the one in the last subsection for generic small γ and large λ. Recall that $\delta\tilde{L}_c^{\text{Regge}}$ likely relates to the discretization artifact. The result suggests that the spinfoam amplitude should suppress the contribution from the discretization artifact, in favor of a good continuum limit.

The complex critical points used in Fig. 14 are likely beyond the stationary phase approximation (for complex action) described above and below (3.7), because these complex critical points do not analytically relate to the real critical point $(\mathring{j}_h, \mathring{g}_{ve}, \mathring{z}_{vf})$ for the flat geometry. It relates to the existence of complex critical points with $\text{Re}(\tilde{\mathcal{S}}) > 0$ in Fig. 14(c1)violating (3.9). Indeed, when we continuously deform the boundary data r' by the deformation by $l_{35} \to l_{35} + \delta l_{35}$ from the boundary data of flat geometry to the one that does not admit flat geometry, the solution of (7.2) and (7.3) deforms analytically from the real critical point to the previous complex critical point $(\delta L_c^{\text{Spinfoam}}, \tilde{Z})(r')$ (see Fig. 13, and the similar property holds for the complex critical points in Sec. VI), but not to any of the complex critical points used in Fig. 14.

The complex critical point used in Fig. 14 has to be studied by the fully-fledged Picard-Lefschetz theory (see, e.g., [22,53,54]). Consequently, given that the spinfoam amplitude is defined on the real integration cycle where $\text{Re}(S) \leq 0$, the complex critical point with $\text{Re}(\tilde{\mathcal{S}}) > 0$ does not contribute to the asymptotics of the amplitude, because the steepest-ascent flow associated to this critical point turns out to have no intersection with the real integration cycle. Therefore, the contributions from the complex critical points in Fig. 15 are vanishing or suppressed for finite or larger γ, where $\text{Re}(S) > 0$ or $e^{\lambda\text{Re}(S)}$ is suppressed.

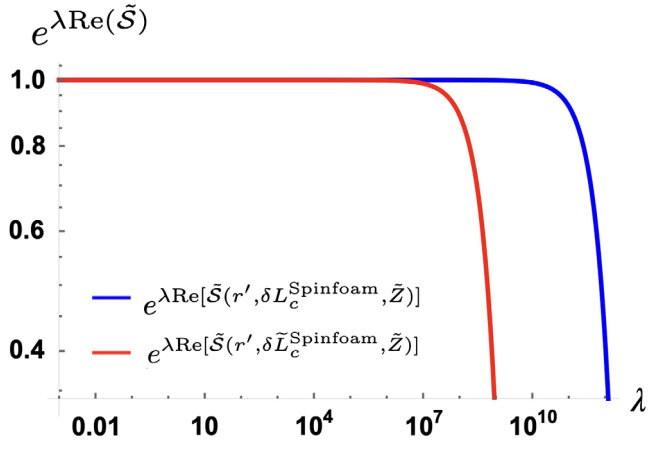

FIG. 15. Figure is the log-log plot of $e^{\lambda\text{Re}[\tilde{\mathcal{S}}(r',\delta L_c^{\text{Spinfoam}},\tilde{Z})]}$ (blue curve) and $e^{\lambda\text{Re}[\tilde{\mathcal{S}}(r',\delta\tilde{L}_c^{\text{Spinfoam}},\tilde{Z})]}$ (red curve) as a function of λ at $\gamma = 10^{-8}$.

VIII. CONCLUSION AND OUTLOOK

Our above analysis demonstrates the importance of complex critical points in understanding the asymptotic behavior of the spinfoam amplitude in the large-j regime. In the case of the four-simplex amplitude, taking into account the complex critical point generalizes the asymptotics to non-Regge boundary data and relates to the twisted geometry. In the case of the simplicial complex, the complex critical point plays an important role in deriving the effective dynamics from the spinfoam amplitude. The effective dynamics closely relate to the Regge gravity in the small-γ regime, as demonstrated by the numerical computation for the amplitude on the double-Δ_3 complex.

In this paper, we examine the semiclassical behavior of the spinfoam amplitude within the regime of large-j. The semiclassical limit characterizes a scenario where the spinfoam amplitude exhibits behavior akin to classical gravity. This limit relates to the region where the values of Planck's constant are small, leading to the emergence of classical behavior. On the other hand, the continuous limit relates to the situation in which a discrete system approaches a continuous or smooth description. This typically involves taking a large number of discrete elements or degrees of freedom and allowing them to become infinitely numerous, resulting in a continuous and infinitely divisible system. It may relate to the situation that the triangulations underlining spinfoams are refined such that the geometries are made by refined Planckian size cells. Note that it is actually possible to relate certain

refinement and small-j spinfoam amplitudes to some semiclassical behaviors, as shown in [55]. Generally speaking, while these two limits are related, they are not interchangeable. For spinfoams, both limits are relevant and may be taken simultaneously. It is indeed possible, as shown in [37,56], where the semiclassical gravity on the continuum is recovered in certain regime with both the large-j and refinement.

Our work provides a general procedure to derive the effective theory in the large-j regime. From the perspective of semiclassical analysis, our numerical computation should be generalized to triangulations larger than double-Δ_3, which has more internal segments. One should check if the Regge gravity still can be reproduced by the large-j effective dynamics on larger triangulations.

The effective dynamics in LQG has been primarily investigated in the context of symmetry-reduced models, such as loop quantum cosmology (LQG) and black holes, see, e.g., [57,58]. The effective dynamics is useful in deriving the singularity resolution. Our result shows that the spinfoam amplitude also results in certain effective dynamics. However, this effective dynamics is in terms of the discrete Regge geometry, in contrast to the effective dynamics in terms of smooth fields in LQC and black holes. A research in progress is to understand if the effective dynamics from the spinfoam amplitude can relate to LQC and black holes. If the relation exists, it might provide a new approach toward embedding LQC and black hole models in the full theory of LQG.

TABLE II. Each cell shows the area of the face shared by line number tetrahedra and column number tetrahedra.

e'	e'_1	e'_2	e'_3	e'_4	e'_5
$\mathring{\mathfrak{a}}_f$					
e					
e_1		5		5	
e_2			2		2
e_3	5			2	
e_4		2			2
e_5	5		2		

It is also interesting to investigate the behavior of the effective dynamics under the lattice refinement for spinfoam amplitudes. The Regge geometries approach to the continuum limit under the refinement, so we expect that the effective dynamics of Regge geometries from spinfoams should reduce to certain effective dynamics of the smooth geometry.

ACKNOWLEDGMENTS

The authors acknowledge the helpful communications with Bianca Dittrich, Carlo Rovelli, and Simone Speziale. M. H. receives support from the National Science Foundation through Grants No. PHY-1912278 and No. PHY-2207763, and the sponsorship provided by the Alexander von Humboldt Foundation during his visit at FAU Erlangen-Nürnberg. In addition, M. H. acknowledges IQG at FAU Erlangen-Nürnberg, IGC at Penn State University, Perimeter Institute for Theoretical Institute, and University of Western Ontario for the hospitality during his visits. Research at Perimeter Institute is supported in part by the Government of Canada through the Department of Innovation, Science and Economic Development and by the Province of Ontario through the Ministry of Colleges and Universities.

APPENDIX A: BOUNDARY DATA FOR SINGLE FOUR-SIMPLEX

In Sec. III, we introduce the real critical points of the four-simplex, which corresponds to the Regge geometry. We construct the Regge boundary geometry, Tables II–IV record areas $\mathring{\mathfrak{a}}_f = \gamma \mathring{j}_f$, 3D normals $\mathring{n}_{ef}$ and the corresponding spinors $\mathring{\xi}_{ef}$ of the single four-simplex.

Tables V and VI record the values of the real critical point $\mathring{g}_{ve}$ and $\mathring{\mathbf{z}}_{vf}$ for the four-simplex with the boundary data $(\mathring{j}_f, \mathring{\xi}_{ef})$.

All the Regge boundary data $\mathring{r} = (\mathring{j}_f, \mathring{\xi}_{ef})$ and the data of the real critical point $(\mathring{g}_{ve}, \mathring{\mathbf{z}}_{vf})$ for the four-simplex amplitude can be found in the Mathematica notebook [59].

TABLE III. Each cell shows the 3D normal vectors of the face shared by line number tetrahedra and column number tetrahedra.

e'	e'_1	e'_2	e'_3	e'_4	e'_5
$\mathring{n}_{ef}$					
e					
e_1		(1.00, 0, 0)	(−0.333, −0.943, 0)	(−0.333, 0.471, −0.816)	(−0.333, 0.471, 0.816)
e_2	(0.938, 0, −0.346)		(−0.782, −0.553, 0.289)	(−0.948, 0.276, −0.160)	(−0.616, 0.276, 0.738)
e_3	(−0.313, −0.884, −0.346)	(0.782, 0.553, 0.289)		(0.0553, 0.986, −0.160)	(−0.0553, 0.673, 0.738)
e_4	(−0.244, 0.345, −0.907)	(0.739, −0.215, 0.639)	(−0.0431, −0.768, 0.639)		(−0.0862, 0.122, 0.989)
e_5	(−0.436, 0.617, 0.655)	(0.859, −0.385, −0.338)	(0.0771, −0.938, −0.338)	(0.154, −0.218, −0.964)	

TABLE IV. Each cell shows a spinor ξ_{ef} corresponding to a 3-normal to the face.

e'	e'_1	e'_2	e'_3	e'_4	e'_5
$\overset{\circ}{\xi}_{ef}$					
e					
e_1		$(0.707, -0.707)$	$(0.707, -0.236 - 0.667\mathrm{i})$	$(0.953, 0.175 - 0.247\mathrm{i})$	$(0.953, -0.175 + 0.247\mathrm{i})$
e_2	$(0.820, -0.572)$		$(0.803, -0.487 - 0.344\mathrm{i})$	$(0.762, 0.622 - 0.181\mathrm{i})$	$(0.932, -0.330 + 0.148\mathrm{i})$
e_3	$(0.572, -0.273 - 0.774\mathrm{i})$	$(0.596, -0.655 - 0.463\mathrm{i})$		$(0.648, 0.043 + 0.761\mathrm{i})$	$(0.362, 0.076 - 0.929\mathrm{i})$
e_4	$(0.976, 0.125 - 0.177\mathrm{i})$	$(0.905, 0.408 - 0.119\mathrm{i})$	$(0.425, 0.051 + 0.904\mathrm{i})$		$(0.997, -0.0432 + 0.0611\mathrm{i})$
e_5	$(0.910, -0.240 + 0.339\mathrm{i})$	$(0.818, -0.525 + 0.236\mathrm{i})$	$(0.576, 0.067 - 0.815\mathrm{i})$	$(0.991, -0.0778 + 0.1100)$	

TABLE V. Each cell of the table is the critical point of $\overset{\circ}{g}_{ve}$.

e	e_1	e_2	e_3	e_4	e_5
$\overset{\circ}{g}_{ve}$	$\begin{pmatrix} 0 & -\mathrm{i} \\ -\mathrm{i} & 0 \end{pmatrix}$	$\begin{pmatrix} 0 & -1.03\mathrm{i} \\ -0.969\mathrm{i} & -0.358\mathrm{i} \end{pmatrix}$	$\begin{pmatrix} 0 & -1.03\mathrm{i} \\ -0.969\mathrm{i} & 0.337 + 0.119\mathrm{i} \end{pmatrix}$	$\begin{pmatrix} 0 & -1.17\mathrm{i} \\ -0.855\mathrm{i} & -0.149 + 0.105\mathrm{i} \end{pmatrix}$	$\begin{pmatrix} 0 & 0.874\mathrm{i} \\ -1.14\mathrm{i} & -0.199 + 0.141\mathrm{i} \end{pmatrix}$

TABLE VI. Each cell shows the critical points of $\overset{\circ}{\mathbf{z}}_{vf}$.

e'	e_1	e_2	e_3	e_4	e_5
$\overset{\circ}{\mathbf{z}}_{vf}$					
e					
e_1		$(1, -1)$		$(1.00, 1.82 + 2.57\mathrm{i})$	
e_2			$(1.00, -0.915 + 0.402\mathrm{i})$		$(1.00, -1.41 - 0.31\mathrm{i})$
e_3	$(1.00, -0.333 + 0.943\mathrm{i})$			$(1.00, 0.086 - 0.690\mathrm{i})$	
e_4		$(1.00, 1.86 + 0.99\mathrm{i})$			$(1.00, 5.72 + 8.08\mathrm{i})$
e_5	$(1.00, -1.82 - 2.57\mathrm{i})$		$(1.00, 0.071 + 0.470\mathrm{i})$		

APPENDIX B: THE NEWTON-RAPHSON METHOD

The Newton-Raphson method for the single-variable equation $f(x) = 0$ is initialized with a starting point x_0, and then one iterate

$$x_{n+1} = x_n - \frac{f(x_n)}{f'(x_n)}, \tag{B1}$$

to approach the solution with higher accuracy. In single four-simplex case as an example, the equations of motion is 44 dimensions, we denote by

$$F\left(\begin{bmatrix} z_1 \\ \vdots \\ z_{44} \end{bmatrix}\right) = \begin{bmatrix} f_1(z_1, \ldots, z_{44}) \\ \vdots \\ f_{44}(z_1, \ldots, z_{44}). \end{bmatrix}. \tag{B2}$$

The derivative of this system is the 44×44 Jacobian given by

$$J(z_1, \ldots, z_{44}) = \begin{bmatrix} \frac{\partial f_1}{\partial z_1} & \cdots & \frac{\partial f_1}{\partial z_{44}} \\ \vdots & \vdots & \vdots \\ \frac{\partial f_{44}}{\partial z_1} & \cdots & \frac{\partial f_{44}}{\partial z_{44}} \end{bmatrix}. \tag{B3}$$

We define the function G by

$$G(z) = z - J(z)^{-1} F(z). \tag{B4}$$

The functional Newton-Raphson method for nonlinear systems is the iteration procedure that evolves from the initial $z^{(0)}$, which in our case is the real critical point $\overset{\circ}{x}$, and generates

$$\begin{aligned} z^{(k)} &= G(z^{(k-1)}) \\ &= z^{(k-1)} - J(z^{(k-1)})^{-1} F(z^{(k-1)}), \qquad k \geq 1. \end{aligned} \tag{B5}$$

We can write this as

$$\begin{bmatrix} z_1^{(k)} \\ \vdots \\ z_{44}^{(k)} \end{bmatrix} = \begin{bmatrix} z_1^{(k-1)} \\ \vdots \\ z_{44}^{(k-1)} \end{bmatrix} + \begin{bmatrix} \Delta z_1^{(k-1)} \\ \vdots \\ \Delta z_{44}^{(k-1)} \end{bmatrix}, \tag{B6}$$

where

$$\begin{bmatrix} \Delta z_1^{(k-1)} \\ \vdots \\ \Delta z_{44}^{(k-1)} \end{bmatrix} = -J(z^{(k-1)})^{-1} F(z^{(k-1)}). \tag{B7}$$

We set the desired tolerance $\epsilon = 10^{-100}$, and we stop after n iterations when

$$\sqrt{\left|(\Delta z_1^{(n-1)})^2 + \cdots + (\Delta z_{44}^{(n-1)})^2\right|} < \epsilon. \tag{B8}$$

The resulting $z^{(n)}$ is the approximated solution within the tolerance. We evaluate the analytic continued four-simplex action $\mathcal{S}$ at $z^{(n)}$ and apply it to the asymptotic formula (3.8).

APPENDIX C: BOUNDARY DATA FOR THE Δ_3^2 COMPLEX

1. Boundary data and the real critical point for the flat Δ_3^2 complex

We construct the flat geometry with the segment lengths in Table I. The corresponding boundary data for flat geometry is shown in Tables VII–XII. Here, the area $\mathfrak{a}_f$ and the spins j_f satisfy $\mathfrak{a}_f = \gamma j_f$.

Once the flat geometry is constructed, the real critical points $(\mathring{j}_h, \mathring{g}_{ve}, \mathring{\mathbf{z}}_{vf})$ can be obtained by solving the critical equations Eqs. (3.1) and (3.2). The solution of the critical point equations relates to the Lorentzian-Regge geometry, as described in [8,9]. $\mathring{g}_{ve}$ relates to the Lorentzian transformation acting on each tetrahedron and gluing them together to form the Δ_3^2 complex. In this model, we fix g_{ve} to be constant $\mathrm{SL}(2,\mathbb{C})$ matrices for $v_1e_5, v_2e_9, v_3e_{12}, v_4e_{16}, v_5e_{19}, v_6e_{21}$. The group elements g_{ve} for the bulk tetrahedra $v_1e_1, v_1e_2, v_2e_6, v_2e_7, v_3e_3, v_3e_{10}, v_4e_{13}, v_5e_{17}, v_6e_{14}$ are fixed to be the upper triangular matrix. For the Δ_3^2 triangulation, there are five internal faces $h(12k)$ with $k = 3, 4, 5, 6, 7$. The areas of these internal faces are shown in Table XIII. The numerical results of the real critical point $(\mathring{g}_{ve}, \mathring{\mathbf{z}}_{vf})$ corresponding to the flat geometry are listed in Tables XIV–XIX.

TABLE VII. Boundary data $(\mathring{\mathfrak{a}}_b, \mathring{\xi}_{eb})$ for the 4-simplex $v_1 = \{1,2,3,4,6\}$.

e'	e'_1	e'_2	e'_3	e'_4	e'_5
$\mathring{\xi}_{eb}$					
e					
e_1					$(-0.41 + 0.73\mathrm{i}, -0.15 - 0.52\mathrm{i})$
e_2				$(-0.61 + 0.22\mathrm{i}, -0.76\mathrm{i})$	
e_3					$(-0.078 - 0.033\mathrm{i}, 0.04 - 1.0\mathrm{i})$
e_4	$(0.60, -0.66 - 0.46\mathrm{i})$		$(0.76, -0.04 - 0.65\mathrm{i})$		
e_5		$(0.43, -0.18 - 0.88\mathrm{i})$		$(0.95, -0.03 + 0.31\mathrm{i})$	

e'	e'_1	e'_2	e'_3	e'_4	e'_5
$\mathring{\mathfrak{a}}_b$					
e					
e_1					0.75
e_2				5	
e_3					0.55
e_4	2		2		
e_5		2.8		2.0	

TABLE VIII. Boundary data $(\overset{\circ}{\mathfrak{a}}_b, \overset{\circ}{\xi}_{eb})$ for the 4-simplex $v_2 = \{1, 2, 3, 5, 6\}$.

e'	e'_2	e'_6	e'_7	e'_8	e'_9
$\overset{\circ}{\xi}_{eb}$					
e					
e_2					$(-0.72 + 0.13\mathrm{i},\ 0.02 - 0.68\mathrm{i})$
e_6				$(0.81\mathrm{i},\ -0.59\mathrm{i})$	
e_7				$(-0.27 - 0.19\mathrm{i},\ -0.94\mathrm{i})$	
e_8	$(0.71,\ -0.24 - 0.67\mathrm{i})$				$(0.95,\ -0.17 + 0.25\mathrm{i})$
e_9		$(0.74,\ -0.67 + 0.05\mathrm{i})$	$(1.0,\ 0.048 - 0.068\mathrm{i})$		

e'	e'_2	e'_6	e'_7	e'_8	e'_9
$\overset{\circ}{\mathfrak{a}}_b$					
e					
e_2					2.8
e_6				5	
e_7				5	
e_8	5				5
e_9		2.6	3.2		

TABLE IX. Boundary data $(\overset{\circ}{\mathfrak{a}}_b, \overset{\circ}{\xi}_{eb})$ for the 4-simplex $v_3 = \{1, 2, 4, 5, 6\}$.

e'	e'_3	e'_7	e'_{10}	e'_{11}	e'_{12}
$\overset{\circ}{\xi}_{eb}$					
e					
e_3				$(-0.22 - 0.03\mathrm{i},\ 0.07 - 0.97\mathrm{i})$	
e_7					$(-0.10 - 0.073\mathrm{i},\ -0.99\mathrm{i})$
e_{10}					$(0.18 + 0.98\mathrm{i},\ 0.065 - 0.11\mathrm{i})$
e_{11}		$(0.98,\ 0.12 - 0.18\mathrm{i})$	$(0.43,\ -0.87 + 0.25\mathrm{i})$		
e_{12}	$(0.99,\ -0.01 - 0.17\mathrm{i})$			$(1.0,\ -0.018 + 0.025\mathrm{i})$	

e'	e'_3	e'_7	e'_{10}	e'_{11}	e'_{12}
$\overset{\circ}{\mathfrak{a}}_b$					
e					
e_3				2	
e_7					3.2
e_{10}					0.69
e_{11}		5	2		
e_{12}	0.55			2	

TABLE X. Boundary data $(\mathring{\mathbf{a}}_b, \mathring{\xi}_{eb})$ for the 4-simplex $v_4 = \{1, 2, 3, 4, 7\}$.

e'	e'_1	e'_{13}	e'_{14}	e'_{15}	e'_{16}
$\mathring{\xi}_{eb}$					
e					
e_1				$(-0.33 + 0.75\mathrm{i},\ -0.11 - 0.56\mathrm{i})$	
e_{13}					$(-0.52 + 0.71\mathrm{i},\ -0.35 - 0.32\mathrm{i})$
e_{14}				$(-0.59 + 0.71\mathrm{i},\ -0.18 - 0.35\mathrm{i})$	
e_{15}		$(0.90,\ -0.14 - 0.41\mathrm{i})$			$(0.63,\ 0.33 + 0.71\mathrm{i})$
e_{16}	$(0.94,\ -0.25 - 0.22\mathrm{i})$		$(0.94,\ 0.28 - 0.18\mathrm{i})$		

e'	e'_1	e'_{13}	e'_{14}	e'_{15}	e'_{16}
$\mathring{\mathbf{a}}_b$					
e					
e_1				2	
e_{13}					3.2
e_{14}			2.1		
e_{15}		5.6			2.3
e_{16}	0.75		0.5		

TABLE XI. Boundary data $(\mathring{\mathbf{a}}_b, \mathring{\xi}_{eb})$ for the 4-simplex $v_5 = \{1, 2, 3, 5, 7\}$.

e'	e'_6	e'_{13}	e'_{17}	e'_{18}	e'_{19}
$\mathring{\xi}_{eb}$					
e					
e_6					$(0.04 + 0.77\mathrm{i},\ 0.01 - 0.63\mathrm{i})$
e_{13}				$(-0.48 + 0.71\mathrm{i},\ -0.31 - 0.41\mathrm{i})$	
e_{17}				$(-0.19 + 0.17\mathrm{i},\ -0.18 - 0.95\mathrm{i})$	$(-0.05 + 0.25\mathrm{i},\ -0.06 - 0.97\mathrm{i})$
e_{18}	$(0.90,\ -0.43)$				
e_{19}		$(0.71,\ -0.26 - 0.65\mathrm{i})$		$(0.95,\ 0.19 + 0.25\mathrm{i})$	

e'	e'_6	e'_{13}	e'_{17}	e'_{18}	e'_{19}
$\mathring{\mathbf{a}}_b$					
e					
e_6					2.6
e_{13}				5.6	
e_{17}				5.4	3.5
e_{18}	5				
e_{19}		3.2		5.2	

All the boundary data $\mathring{r} = (\mathring{j}_b, \mathring{\xi}_{eb})$ and the data of the real critical point $(\mathring{j}_h, \mathring{g}_{ve}, \mathring{\mathbf{z}}_{vf})$ can be found in the Mathematica notebook in [59].

2. Boundary data and the pseudocritical points for the curved Δ_3^2 complex

The boundary data in Appendix C 1 admits a flat geometry. To construct a curved geometry, we deform the segment length $l_{35} \to l_{35} + 10^{-3}$ and keep the other boundary segment lengths unchanged. We list the boundary data for this curved geometry in Tables XX–XXV as the internal segment length is $l_{12} = L_0 + \delta L_c^{\mathrm{Regge}}$.

The curved geometry does not have real critical point. However, we can find the pseudocritical point $(j_h^0, g_{ve}^0, \mathbf{z}_{vf}^0)$, which is close to the real critical point inside the real integration domain. The pseudocritical point satisfies the critical equation (3.1) but violates the critical equation (3.2).

TABLE XII. Boundary data $(\overset{\circ}{\mathbf{a}}_b, \overset{\circ}{\xi}_{eb})$ for the 4-simplex $v_6 = \{1, 2, 4, 5, 7\}$.

e'	e'_{10}	e'_{14}	e'_{17}	e'_{20}	e'_{21}
$\overset{\circ}{\xi}_{eb}$					
e					
e_{10}				$(0.20 + 0.91\text{i},\ 0.07 - 0.35\text{i})$	
e_{14}					$(-0.55 + 0.68\text{i},\ -0.16 - 0.46\text{i})$
e_{17}					
e_{20}		$(0.76,\ 0.22 - 0.61\text{i})$	$(0.74,\ 0.57 - 0.36\text{i})$		$(0.85,\ 0.52 - 0.1\text{i})$
e_{21}	$(0.95,\ -0.31 + 0.07\text{i})$		$(0.39,\ 0.89 - 0.23\text{i})$		

e'	e'_{10}	e'_{14}	e'_{17}	e'_{20}	e'_{21}
$\overset{\circ}{\mathbf{a}}_b$					
e					
e_{10}				2	
e_{14}					0.5
e_{17}					
e_{20}		2.1	5.4		2.4
e_{21}	0.69		3.5		

TABLE XIII. Areas of internal faces h in Δ^2_3 complex.

$\mathbf{a}_{h(123)}$	$\mathbf{a}_{h(124)}$	$\mathbf{a}_{h(125)}$	$\mathbf{a}_{h(126)}$	$\mathbf{a}_{h(127)}$
0.971	0.333	1.55	1.78	1.93

TABLE XIV. The real critical point $(\overset{\circ}{g}_{ve}, \overset{\circ}{\mathbf{z}}_{vf})$ for the 4-simplex $v_1 = (1, 2, 3, 4, 6)$.

e	e_1	e_2	e_3
$\overset{\circ}{g}_{v_1 e}$	$\begin{pmatrix} 0.96 & 0.42 + 0.04\text{i} \\ 0 & 1 \end{pmatrix}$	$\begin{pmatrix} 0.99 & -0.05 - 0.15\text{i} \\ 0 & 1 \end{pmatrix}$	$\begin{pmatrix} 0.77 & -0.13 - 0.72\text{i} \\ 0 & 1.3 \end{pmatrix}$
e	e_4	e_5	
$\overset{\circ}{g}_{v_1 e}$	$\begin{pmatrix} 0 & -1.0\text{i} \\ -0.97\text{i} & 0.34 + 0.12\text{i} \end{pmatrix}$	$\begin{pmatrix} 0 & -1.1\text{i} \\ -0.91\text{i} & 0.46 + 0.12\text{i} \end{pmatrix}$	

e'	e'_1	e'_2	e'_3	e'_4	e'_5
$\lvert\overset{\circ}{\mathbf{z}}_{v_1 f}\rangle$					
e					
e_1			$(1, -0.94 + 0.69\text{i})$		$(1, -0.82 + 0.45\text{i})$
e_2	$(1, 0.87 - 0.49\text{i})$			$(1, -0.33 + 0.94\text{i})$	
e_3		$(1, -0.1 + 1.5\text{i})$			$(1, 2.5 + 6.0\text{i})$
e_4	$(1, -0.92 + 0.40\text{i})$		$(1, 0.3 + 2.1\text{i})$		
e_5		$(1, -0.14 + 0.75\text{i})$		$(1, 0.2 - 1.4\text{i})$	

TABLE XV. The real critical point $(\overset{\circ}{g}_{ve}, \overset{\circ}{\mathbf{z}}_{vf})$ for the 4-simplex $v_2 = (1,2,3,5,6)$.

e	e_2	e_6	e_7
$\overset{\circ}{g}_{v_2 e}$	$\begin{pmatrix} 0.99 & -0.05-0.15\mathrm{i} \\ 0.99 & -0.05-0.15\mathrm{i} \end{pmatrix}$	$\begin{pmatrix} 0.98 & 0.32 \\ 0 & 1 \end{pmatrix}$	$\begin{pmatrix} 1.0 & -0.031+0.044\mathrm{i} \\ 0 & 0.96 \end{pmatrix}$
e	e_8	e_9	
$\overset{\circ}{g}_{v_2 e}$	$\begin{pmatrix} 0 & -1.0\mathrm{i} \\ -1.0\mathrm{i} & 0 \end{pmatrix}$	$\begin{pmatrix} 1.26 & 0.09-0.13\mathrm{i} \\ 0.09+0.13\mathrm{i} & 0.82 \end{pmatrix}$	

e'	e'_2	e'_6	e'_7	e'_8	e'_9
$\lvert\overset{\circ}{\mathbf{z}}_{v_2 f}\rangle$					
e					
e_2			$(1,-0.1+1.5\mathrm{i})$		$(1,-0.14+0.75\mathrm{i})$
e_6	$(1,0.87-0.49\mathrm{i})$			$(1,0.87-0.49\mathrm{i})$	
e_7		$(1,-0.86-0.07\mathrm{i})$		$(1,1.8+2.6\mathrm{i})$	
e_8	$(1,-0.33+0.94\mathrm{i})$				$(1,-1.8-2.6\mathrm{i})$
e_9		$(1,-1.09-0.05\mathrm{i})$	$(1,4.9+7.0\mathrm{i})$		

The data for the pseudocritical point is listed in Tables XXVI–XXXI.

The boundary data for the curved geometry and the corresponding pseudocritical point can be found in Mathematica notebook [59].

APPENDIX D: REGGE ACTION

Let us first recall the volume of the simplex. The volume formula for the Lorentzian four-simplex σ is given by [60,61]

$$\mathbb{V}_\sigma = \frac{(-1)^4}{2^4(4!)^2}\det(\mathbf{C}_\sigma), \tag{D1}$$

where $\mathbb{V}_\sigma$ is the volume square and $\det(\mathbf{C}_\sigma)$ is the Cayley-Menger determinant. The Cayley-Menger matrix $\mathbf{C}_\sigma$ is the 6×6 matrix with entries l_{ij}^2 for $i,j = 0,\ldots,4$, where l_{ij} is the segment length. The Cayley-Menger matrix is augmented by an additional row and column with entries given by $(\mathbf{C}_\sigma)_{5,5} = 0$ and $(\mathbf{C}_\sigma)_{i,5} = (\mathbf{C}_\sigma)_{5,j} = 1$. That is

$$\mathbf{C}_\sigma = \left[\begin{array}{c|c} l_{ij}^2 & 1_i \\ \hline 1_j & 0 \end{array}\right] \tag{D2}$$

Similarly, the volume formula of the Euclidean tetrahedron is given by

TABLE XVI. The real critical point $(\overset{\circ}{g}_{ve}, \overset{\circ}{\mathbf{z}}_{vf})$ for the 4-simplex $v_3 = (1,2,4,5,6)$.

e	e_3	e_7	e_{10}
$\overset{\circ}{g}_{v_3 e}$	$\begin{pmatrix} 0.77 & -0.13-0.72\mathrm{i} \\ 0 & 1.3 \end{pmatrix}$	$\begin{pmatrix} 1.0 & -0.031+0.044\mathrm{i} \\ 0 & 0.96 \end{pmatrix}$	$\begin{pmatrix} 0.96 & 0.38 \\ 0 & 1 \end{pmatrix}$
e	e_{11}	e_{12}	
$\overset{\circ}{g}_{v_3 e}$	$\begin{pmatrix} 0 & -1.2\mathrm{i} \\ -0.86\mathrm{i} & -0.15+0.11\mathrm{i} \end{pmatrix}$	$\begin{pmatrix} 0 & -1.8\mathrm{i} \\ -0.55\mathrm{i} & -0.16+0.12\mathrm{i} \end{pmatrix}$	

e'	e'_3	e'_7	e'_{10}	e'_{11}	e'_{12}
$\lvert\overset{\circ}{z}_{v_3 f}\rangle$					
e					
e_3			$(1,-0.94+0.69\mathrm{i})$	$(1,0.3+2.1\mathrm{i})$	
e_7	$(1,-0.1+1.5\mathrm{i})$				$(1,4.9+7.0\mathrm{i})$
e_{10}		$(1,-0.86-0.07\mathrm{i})$			$(1,-0.45-0.08\mathrm{i})$
e_{11}		$(1,1.8+2.6\mathrm{i})$	$(1,-0.68-0.15\mathrm{i})$		
e_{12}	$(1,2.5+6.0\mathrm{i})$			$(1,5.7+8.1\mathrm{i})$	

TABLE XVII. The real critical point $(\overset{\circ}{g}_{ve}, \overset{\circ}{\mathbf{z}}_{vf})$ for the 4-simplex $v_4 = (1,2,3,4,7)$.

e	e_1	e_{13}	e_{14}
$\overset{\circ}{g}_{v_4 e}$	$\begin{pmatrix} 0.96 & 0.42+0.04\mathrm{i} \\ 0 & 1 \end{pmatrix}$	$\begin{pmatrix} 0.84 & 0.82+0.19\mathrm{i} \\ 0 & 1.2 \end{pmatrix}$	$\begin{pmatrix} 0.68 & 1.3+0.9\mathrm{i} \\ 0 & 1.5 \end{pmatrix}$
e	e_{15}	e_{16}	
$\overset{\circ}{g}_{v_4 e}$	$\begin{pmatrix} 0 & -1.3\mathrm{i} \\ -0.79\mathrm{i} & -0.34-0.92\mathrm{i} \end{pmatrix}$	$\begin{pmatrix} 0 & -1.3\mathrm{i} \\ -0.77\mathrm{i} & -0.49-1.01\mathrm{i} \end{pmatrix}$	

e'	e'_1	e'_{13}	e'_{14}	e'_{15}	e'_{16}
$\lvert\overset{\circ}{z}_{v_4 f}\rangle$					
e					
e_1		$(1, 0.87-0.49\mathrm{i})$		$(1, -0.92+0.40\mathrm{i})$	
e_{13}			$(1, -0.92+0.75\mathrm{i})$		$(1, -0.73+0.54\mathrm{i})$
e_{14}	$(1, -0.94+0.69\mathrm{i})$			$(1, -0.94+0.77\mathrm{i})$	
e_{15}		$(1, -0.83+0.56\mathrm{i})$			$(1, -1.1-1.2\mathrm{i})$
e_{16}	$(1, -0.82+0.45\mathrm{i})$		$(1, -1.0+0.81\mathrm{i})$		

TABLE XVIII. The real critical point $(\overset{\circ}{g}_{ve}, \overset{\circ}{\mathbf{z}}_{vf})$ for the 4-simplex $v_5 = (1,2,3,5,7)$.

e	e_6	e_{13}	e_{17}
$\overset{\circ}{g}_{v_5 e}$	$\begin{pmatrix} 0.98 & 0.32 \\ 0 & 1 \end{pmatrix}$	$\begin{pmatrix} 0.84 & 0.82+0.19\mathrm{i} \\ 0 & 1.2 \end{pmatrix}$	$\begin{pmatrix} 0.84 & 0.73-0.05\mathrm{i} \\ 0 & 1.2 \end{pmatrix}$
e	e_{18}	e_{19}	
$\overset{\circ}{g}_{v_5 e}$	$\begin{pmatrix} 0 & -1.1\mathrm{i} \\ -0.88\mathrm{i} & -0.72\mathrm{i} \end{pmatrix}$	$\begin{pmatrix} 0 & -1.2\mathrm{i} \\ -0.86\mathrm{i} & 0.03-0.72\mathrm{i} \end{pmatrix}$	

e'	e'_6	e'_{13}	e'_{17}	e'_{18}	e'_{19}
$\lvert\overset{\circ}{z}_{v_5 f}\rangle$					
e					
e_6			$(1, -0.86-0.07\mathrm{i})$		$(1, -1.09-0.05\mathrm{i})$
e_{13}	$(1, 0.87-0.49\mathrm{i})$			$(1, -0.83+0.56\mathrm{i})$	
e_{17}		$(1, -0.92+0.75\mathrm{i})$			$(1, 1, -3.2+0.6\mathrm{i})$
e_{18}	$(1, -1)$		$(1, -1.9+2.2\mathrm{i})$		
e_{19}		$(1, -0.73+0.54\mathrm{i})$		$(1, -1.8-0.8\mathrm{i})$	

$$\mathbb{V}_\tau = \frac{(-1)^{3+1}}{2^3(3!)^2}\det(\mathbf{C}_\tau) \tag{D3}$$

here, $\mathbf{C}_\tau$ is the Cayley-Menger matrix for the tetrahedron, which is a 5×5 matrix defined similarly as the above.

Given $\vec{a}$ and $\vec{b}$ as timelike normal vector of two tetrahedra τ_a, τ_b of the four-simplex σ, the Lorentzian dihedral angles are [62,63]

$$\theta_t(\sigma) = \mathrm{sgn}(\vec{a}\cdot\vec{b})\cosh^{-1}\left(\mathrm{sgn}(\vec{a}\cdot\vec{b})\frac{\vec{a}\cdot\vec{b}}{|\vec{a}||\vec{b}|}\right),$$
$$\mathrm{sgn}(\vec{a}\cdot\vec{b}) = \frac{\sqrt{(\vec{a}\cdot\vec{b})^2}}{\vec{a}\cdot\vec{b}}. \tag{D4}$$

In the four-dimentional triangulation, the hinge of the angle is a triangle denoted by t. Given a triangle t, it is shared by τ_a and τ_b, and $s_{\bar{t}}$ is the length square of the segment opposite to the triangle t in σ. For example, in the four-simplex $\sigma = (12345)$, the tetrahedra $\tau_a = (1234)$ and $\tau_b = (1235)$ share the triangle $t = (123)$. Then $\bar{t}$ is the segment (45). The dihedral angles with respect to t are given by [64]

$$\theta_t(\sigma) = \frac{\sqrt{\left(\frac{1}{\mathbb{V}_t}\frac{\partial\mathbb{V}_\sigma}{\partial s_{\bar{t}}}\right)^2}}{\frac{1}{\mathbb{V}_t}\frac{\partial\mathbb{V}_\sigma}{\partial s_{\bar{t}}}}\cosh^{-1}\left(\frac{\sqrt{\left(\frac{1}{\mathbb{V}_t}\frac{\partial\mathbb{V}_\sigma}{\partial s_{\bar{t}}}\right)^2}}{\frac{1}{\mathbb{V}_t}\frac{\partial\mathbb{V}_\sigma}{\partial s_{\bar{t}}}}\frac{\frac{3^2\cdot 4^2}{\mathbb{V}_t}\frac{\partial\mathbb{V}_\sigma}{\partial s_{\bar{t}}}}{\sqrt{3^2\frac{\mathbb{V}_{\tau_a}}{\mathbb{V}_t}}\sqrt{3^2\frac{\mathbb{V}_{\tau_b}}{\mathbb{V}_t}}}\right) \tag{D5}$$

TABLE XIX. The real critical point $(\overset{\circ}{g}_{ve}, \overset{\circ}{\mathbf{z}}_{vf})$ for the 4-simplex $v_6 = (1,2,4,5,7)$.

e	e_{10}	e_{14}	e_{17}
$\overset{\circ}{g}_{v_6 e}$	$\begin{pmatrix} 0.96, 0.38 & \\ 0 & 1 \end{pmatrix}$	$\begin{pmatrix} 0.68 & 1.3+0.9\mathrm{i} \\ 0 & 1.5 \end{pmatrix}$	$\begin{pmatrix} 0.84 & 0.73-0.05\mathrm{i} \\ 0 & 1.2 \end{pmatrix}$
e	e_{20}	e_{21}	
$\overset{\circ}{g}_{v_6 e}$	$\begin{pmatrix} 0 & -1.1\mathrm{i} \\ -0.93\mathrm{i} & -0.17-0.96\mathrm{i} \end{pmatrix}$	$\begin{pmatrix} 0 & -1.2\mathrm{i} \\ -0.84\mathrm{i} & 0.4-2.3\mathrm{i} \end{pmatrix}$	

e'	e'_{10}	e'_{14}	e'_{17}	e'_{20}	e'_{21}
$\lvert\overset{\circ}{z}_{v_6 f}\rangle$					
e					
e_{10}		$(1, -0.94+0.69\mathrm{i})$		$(1, -0.68-0.15\mathrm{i})$	
e_{14}			$(1, -0.92+0.75\mathrm{i})$		$(1, -1+0.81\mathrm{i})$
e_{17}	$(1, -0.86-0.07\mathrm{i})$			$(1, -1.9+2.2\mathrm{i})$	
e_{20}		$(1, -0.94+0.77\mathrm{i})$			$(1, -2.7-0.4\mathrm{i})$
e_{21}	$(1, -0.45-0.08\mathrm{i})$		$(1, -3.2+0.6\mathrm{i})$		

TABLE XX. Boundary data $(\mathfrak{a}_b, \xi_{eb})$ of the curved geometry for the four-simplex $v_1 = \{1,2,3,4,6\}$.

e'	e'_1	e'_2	e'_3	e'_4	e'_5
ξ_{eb}					
e					
e_1					$(-0.40+0.73\mathrm{i},\ -0.15-0.53\mathrm{i})$
e_2				$(-0.61+0.22\mathrm{i},\ -0.76\mathrm{i})$	
e_3					$(-0.079-0.033\mathrm{i},\ 0.04-1.0\mathrm{i})$
e_4	$(0.60,\ -0.66-0.46\mathrm{i})$		$(0.76,\ -0.04-0.65\mathrm{i})$		
e_5		$(0.43,\ -0.18-0.88\mathrm{i})$		$(0.95,\ -0.03+0.31\mathrm{i})$	

e'	e'_1	e'_2	e'_3	e'_4	e'_5
$\mathfrak{a}_b$					
e					
e_1					0.75
e_2				5	
e_3					0.55
e_4	2		2		
e_5		2.8		2.0	

Here, $\mathbb{V}$ are volume square ($\mathbb{V}_t = \mathfrak{a}_t^2$ is the area square) and s is length square. As we only consider the spacelike triangles and tetrahedra, so all the volume square are positive. The above formula can be simplified as

$$\theta_t(\sigma) = \frac{\sqrt{\left(\frac{1}{\mathbb{V}_t}\frac{\partial \mathbb{V}_\sigma}{\partial s_{\bar{t}}}\right)^2}}{\frac{1}{\mathbb{V}_t}\frac{\partial \mathbb{V}_\sigma}{\partial s_{\bar{t}}}} \cosh^{-1}\left(\frac{4^2\sqrt{\left(\frac{1}{\mathbb{V}_t}\frac{\partial \mathbb{V}_\sigma}{\partial s_{\bar{t}}}\right)^2}}{\sqrt{\mathbb{V}_{\tau_a}}\sqrt{\mathbb{V}_{\tau_b}}}\right). \tag{D6}$$

Here, the volume of four-simplex, tetrahedra and areas of triangles can be computed by following Eqs. (D1) and (D3). Given any simplicial complex $\mathcal{K}$, Regge action can be defined as

$$S_{\mathrm{Regge}} = \sum_{\sigma \subset \mathcal{K}} \sum_{t \subset \sigma} \mathfrak{a}_t \theta_t(\sigma), \tag{D7}$$

where $\mathfrak{a}_t$ are the areas of the triangles t and θ_t is the dihedral angle of triangle t.

TABLE XXI. Boundary data $(\mathfrak{a}_b, \xi_{eb})$ of the curved geometry for the four-simplex $v_2 = \{1, 2, 3, 5, 6\}$.

e'	e'_2	e'_6	e'_7	e'_8	e'_9
ξ_{eb}					
e					
e_2					$(-0.71 + 0.13\text{i},\ 0.02 - 0.69\text{i})$
e_6				$(0.81\text{i},\ -0.59\text{i})$	
e_7				$(-0.27 - 0.19\text{i},\ -0.94\text{i})$	
e_8	$(0.71,\ -0.24 - 0.67\text{i})$				$(0.95,\ -0.17 + 0.25\text{i})$
e_9		$(0.74,\ -0.67 + 0.05\text{i})$	$(1.0,\ 0.049 - 0.065\text{i})$		

e'	e'_2	e'_6	e'_7	e'_8	e'_9
$\mathfrak{a}_b$					
e					
e_2					2.8
e_6				5	
e_7				5	
e_8	5				5
e_9		2.6	3.2		

TABLE XXII. Boundary data $(\mathfrak{a}_b, \xi_{eb})$ of curved geometry for the four-simplex $v_3 = \{1, 2, 4, 5, 6\}$.

e'	e'_3	e'_7	e'_{10}	e'_{11}	e'_{12}
ξ_{eb}					
e					
e_3				$(-0.22 - 0.03\text{i},\ 0.07 - 0.97\text{i})$	
e_7					$(-0.105 - 0.072\text{i},\ -0.99\text{i})$
e_{10}					$(0.18 + 0.98\text{i},\ 0.065 - 0.106\text{i})$
e_{11}		$(0.98,\ 0.12 - 0.18\text{i})$	$(0.43,\ -0.87 + 0.25\text{i})$		
e_{12}	$(0.99,\ -0.01 - 0.17\text{i})$			$(1.0,\ -0.018 + 0.025\text{i})$	

e'	e'_3	e'_7	e'_{10}	e'_{11}	e'_{12}
$\mathfrak{a}_b$					
e					
e_3				2.0	
e_7					3.2
e_{10}					0.69
e_{11}		5	2		
e_{12}	0.55			2	

TABLE XXIII. Boundary data $(\mathfrak{a}_b, \xi_{eb})$ of curved geometry for the four-simplex $v_4 = \{1, 2, 3, 4, 7\}$.

e'	e'_1	e'_{13}	e'_{14}	e'_{15}	e'_{16}
ξ_{eb}					
e					
e_1				$(-0.33 + 0.75\text{i},\ -0.12 - 0.57\text{i})$	
e_{13}					$(-0.52 + 0.71\text{i},\ -0.35 - 0.32\text{i})$
e_{14}				$(-0.58 + 0.71\text{i},\ -0.19 - 0.35\text{i})$	
e_{15}		$(0.90,\ -0.14 - 0.41\text{i})$			$(0.63,\ 0.33 + 0.71\text{i})$
e_{16}	$(0.94,\ -0.25 - 0.22\text{i})$		$(0.94,\ 0.28 - 0.18\text{i})$		

e'	e'_1	e'_{13}	e'_{14}	e'_{15}	e'_{16}
$\mathfrak{a}_b$					
e					
e_1				2	
e_{13}					3.2
e_{14}			2.1		
e_{15}		5.6			2.3
e_{16}	0.75		0.5		

TABLE XXIV. Boundary data $(\mathfrak{a}_b, \xi_{eb})$ of the curved geometry for the 4-simplex $v_5 = \{1, 2, 3, 5, 7\}$.

e'	e'_6	e'_{13}	e'_{17}	e'_{18}	e'_{19}
ξ_{eb}					
e					
e_6					$(0.04 + 0.77\text{i},\ 0.01 - 0.64\text{i})$
e_{13}				$(-0.48 + 0.71\text{i},\ -0.31 - 0.41\text{i})$	
e_{17}				$(-0.19 + 0.17\text{i},\ -0.18 - 0.95\text{i})$	$(-0.05 + 0.25\text{i},\ -0.05 - 0.97\text{i})$
e_{18}	$(0.90,\ -0.43)$				
e_{19}		$(0.71,\ -0.26 - 0.66\text{i})$		$(0.95,\ 0.19 + 0.24\text{i})$	

e'	e'_6	e'_{13}	e'_{17}	e'_{18}	e'_{19}
$\mathfrak{a}_b$					
e					
e_6					2.6
e_{13}				5.6	
e_{17}				5.4	3.5
e_{18}	5				
e_{19}		3.2		5.2	

TABLE XXV. Boundary data $(\mathfrak{a}_b, \xi_{eb})$ of the curved geometry for the four-simplex $v_6 = \{1, 2, 4, 5, 7\}$.

e'	e'_{10}	e'_{14}	e'_{17}	e'_{20}	e'_{21}
ξ_{eb}					
e					
e_{10}				$(0.20 + 0.91\text{i},\ 0.07 - 0.35\text{i})$	
e_{14}					$(-0.55 + 0.68\text{i},\ -0.16 - 0.47\text{i})$
e_{17}					
e_{20}		$(0.76,\ 0.22 - 0.61\text{i})$	$(0.74,\ 0.57 - 0.36\text{i})$		$(0.85,\ 0.52 - 0.1\text{i})$
e_{21}	$(0.95,\ -0.31 + 0.07\text{i})$		$(0.39,\ 0.89 - 0.23\text{i})$		

e'	e'_{10}	e'_{14}	e'_{17}	e'_{20}	e'_{21}
$\mathfrak{a}_b$					
e					
e_{10}				2	
e_{14}					0.5
e_{17}					
e_{20}		2.1	5.4		2.4
e_{21}	0.69		3.5		

TABLE XXVI. The pseudocritical point $(g^0_{ve}, \mathbf{z}^0_{vf})$ for the four-simplex $v_1 = (1, 2, 3, 4, 6)$.

e	e_1	e_2	e_3
$g^0_{v_1 e}$	$\begin{pmatrix} 0.96 & 0.40 + 0.02i \\ 0 & 1 \end{pmatrix}$	$\begin{pmatrix} 0.99 & -0.06 - 0.16i \\ 0 & 1 \end{pmatrix}$	$\begin{pmatrix} 0.78 & -0.12 - 0.71i \\ -0.00024 - 0.00065i & 1.29 \end{pmatrix}$
e	e_4	e_5	
$g^0_{v_1 e}$	$\begin{pmatrix} -0.0016 - 0.0001i & -1.0i \\ -0.97i & 0.34 + 0.12i \end{pmatrix}$	$\begin{pmatrix} 0 & -1.1\text{i} \\ -0.91\text{i} & 0.46 + 0.12\text{i} \end{pmatrix}$	

e'	e'_1	e'_2	e'_3	e'_4	e'_5
$\lvert\mathbf{z}^0_{v_1 f}\rangle$					
e					
e_1			$(1, -0.95 + 0.70\text{i})$		$(1, -0.82 + 0.45\text{i})$
e_2	$(1, 0.87 - 0.50\text{i})$			$(1, -0.34 + 0.95\text{i})$	
e_3		$(1, -0.1 + 1.5\text{i})$			$(1, 2.5 + 6.0\text{i})$
e_4	$(1, -0.92 + 0.40\text{i})$		$(1, 0.3 + 2.1\text{i})$		
e_5		$(1, -0.14 + 0.75\text{i})$		$(1, 0.2 - 1.4\text{i})$	

TABLE XXVII. The pseudocritical point $(g^0_{ve}, \mathbf{z}^0_{vf})$ for the four-simplex $v_2 = (1, 2, 3, 5, 6)$.

e	e_2	e_6	e_7
$g^0_{v_2e}$	$\begin{pmatrix} 0.99 & -0.05-0.15i \\ 0.0024-0.0112i & 1.01 \end{pmatrix}$	$\begin{pmatrix} 0.98 & 0.30 \\ 0 & 1 \end{pmatrix}$	$\begin{pmatrix} 1.0 & -0.029+0.048i \\ 0 & 0.97 \end{pmatrix}$
e	e_8	e_9	
$g^0_{v_2e}$	$\begin{pmatrix} 0.0008+0.00056i & -1.0i \\ -1.0i & -0.0054-0.0011i \end{pmatrix}$	$\begin{pmatrix} 0 & -0.98i \\ -1.0i & 0.029+0.016i \end{pmatrix}$	

e'	e'_2	e'_6	e'_7	e'_8	e'_9
$\lvert\mathbf{z}^0_{v_2f}\rangle$					
e					
e_2			$(1, -0.1+1.5\text{i})$		$(1, -0.14+0.75\text{i})$
e_6	$(1, 0.87-0.48\text{i})$			$(1, -1)$	
e_7		$(1, -0.86-0.07\text{i})$		$(1, 1.8+2.6\text{i})$	
e_8	$(1, -0.33+0.94\text{i})$				$(1, -1.8-2.6\text{i})$
e_9		$(1, -1.09-0.05\text{i})$	$(1, 4.7+6.9\text{i})$		

TABLE XXVIII. The real critical point $(g^0_{ve}, \mathbf{z}^0_{vf})$ for the four-simplex $v_3 = (1, 2, 4, 5, 6)$.

e	e_3	e_7	e_{10}
$g^0_{v_3e}$	$\begin{pmatrix} 0.78 & -0.13-0.72i \\ 0 & 1.29 \end{pmatrix}$	$\begin{pmatrix} 1.04 & -0.030+0.046i \\ -0.0010+0.0018i & 0.96 \end{pmatrix}$	$\begin{pmatrix} 0.96 & 0.38 \\ 0 & 1 \end{pmatrix}$
e	e_{11}	e_{12}	
$g^0_{v_3e}$	$\begin{pmatrix} -0.00013-0.0001i & -1.2i \\ -0.85i & -0.15+0.11i \end{pmatrix}$	$\begin{pmatrix} 0 & -1.8i \\ -0.55i & -0.16+0.12i \end{pmatrix}$	

e'	e'_3	e'_7	e'_{10}	e'_{11}	e'_{12}
$\lvert\mathbf{z}^0_{v_3f}\rangle$					
e					
e_3			$(1, -0.94+0.69\text{i})$	$(1, 0.3+2.1\text{i})$	
e_7	$(1, -0.1+1.5\text{i})$				$(1, 4.9+7.0\text{i})$
e_{10}		$(1, -0.86-0.07\text{i})$			$(1, -0.45-0.08\text{i})$
e_{11}		$(1, 1.8+2.6\text{i})$	$(1, -0.68-0.15\text{i})$		
e_{12}	$(1, 2.5+6.0\text{i})$			$(1, 5.7+8.1\text{i})$	

TABLE XXIX. The pseudocritical point (g^0_{ve}, z^0_{vf}) for the four-simplex $v_4 = (1,2,3,4,7)$.

e	e_1	e_{13}	e_{14}
$g^0_{v_4e}$	$\begin{pmatrix} 0.96 & 0.42+0.04i \\ 0.02-0.02i & 1.05 \end{pmatrix}$	$\begin{pmatrix} 0.84 & 0.82+0.2i \\ 0 & 1.2 \end{pmatrix}$	$\begin{pmatrix} 0.68 & 1.3+0.9i \\ -0.0023+0.0038i & 1.5+0.01i \end{pmatrix}$
e	e_{15}	e_{16}	
$g^0_{v_4e}$	$\begin{pmatrix} 0.0032-0.0015i & -1.3i \\ -0.79i & -0.34-0.92i \end{pmatrix}$	$\begin{pmatrix} 0 & -1.3i \\ -0.77i & -0.49-1.01i \end{pmatrix}$	

e'	e'_1	e'_{13}	e'_{14}	e'_{15}	e'_{16}
$\lvert\mathbf{z}^0_{v_4f}\rangle$					
e					
e_1		$(1, 0.88-0.46\text{i})$		$(1, -0.91+0.40\text{i})$	
e_{13}			$(1, -0.92+0.75\text{i})$		$(1, -0.73+0.54\text{i})$
e_{14}	$(1, -0.94+0.68\text{i})$			$(1, -0.94+0.77\text{i})$	
e_{15}		$(1, -0.83+0.56\text{i})$			$(1, -1.1-1.2\text{i})$
e_{16}	$(1, -0.82+0.45\text{i})$		$(1, -1.0+0.81\text{i})$		

TABLE XXX. The pseudocritical point $(g^0_{ve}, \mathbf{z}^0_{vf})$ for the four-simplex $v_5 = (1,2,3,5,7)$.

e	e_6	e_{13}	e_{17}
$g^0_{v_5e}$	$\begin{pmatrix} 0.98 & 0.32 \\ 0.011+0.006i & 1.03 \end{pmatrix}$	$\begin{pmatrix} 0.84 & 0.82+0.19i \\ -0.0012+0.011i & 1.19 \end{pmatrix}$	$\begin{pmatrix} 0.84 & 0.73-0.05\text{i} \\ 0 & 1.2 \end{pmatrix}$
e	e_{18}	e_{19}	
$g^0_{v_5e}$	$\begin{pmatrix} -0.00066+0.00052 & -1.1i \\ -0.88i & -0.72i \end{pmatrix}$	$\begin{pmatrix} 0 & -1.2i \\ -0.86i & 0.03-0.72i \end{pmatrix}$	

e'	e'_6	e'_{13}	e'_{17}	e'_{18}	e'_{19}
$\lvert\mathbf{z}^0_{v_5f}\rangle$					
e					
e_6			$(1, -0.86-0.07\text{i})$		$(1, -1.09-0.06\text{i})$
e_{13}	$(1, 0.87-0.50\text{i})$			$(1, -0.83+0.56\text{i})$	
e_{17}		$(1, -0.93+0.75\text{i})$			$(1, 1, -3.2+0.6\text{i})$
e_{18}	$(1, -1)$		$(1, -2+2.2\text{i})$		
e_{19}		$(1, -0.73+0.54\text{i})$		$(1, -1.8-0.8\text{i})$	

TABLE XXXI. The pseudocritical point $(g^0_{ve}, \mathbf{z}^0_{vf})$ for the four-simplex $v_6 = (1, 2, 4, 5, 7)$.

e	e_{10}	e_{14}	e_{17}
$g^0_{v_6e}$	$\begin{pmatrix} 0.96, 0.38 & \\ 0.00077 + 0.00070i & 1.05 \end{pmatrix}$	$\begin{pmatrix} 0.68 & 1.3 + 0.9i \\ 0 & 1.5 \end{pmatrix}$	$\begin{pmatrix} 0.83 & 0.73 - 0.05i \\ -0.0014 - 0.0019i & 1.2 \end{pmatrix}$
e	e_{20}	e_{21}	
$g^0_{v_6e}$	$\begin{pmatrix} -0.00019 - 0.00100i & -1.1i \\ -0.93i & 0.17 - 0.96i \end{pmatrix}$	$\begin{pmatrix} 0 & -1.2\text{i} \\ -0.84\text{i} & 0.4 - 2.3\text{i} \end{pmatrix}$	

e'	e'_{10}	e'_{14}	e'_{17}	e'_{20}	e'_{21}
$\lvert\mathbf{z}^0_{v_6f}\rangle$					
e					
e_{10}		$(1, -0.94 + 0.68\text{i})$		$(1, -0.68 - 0.15\text{i})$	
e_{14}			$(1, -0.92 + 0.75\text{i})$		$(1, -1 + 0.81\text{i})$
e_{17}	$(1, -0.86 - 0.07\text{i})$			$(1, -1.9 + 2.2\text{i})$	
e_{20}		$(1, -0.94 + 0.77\text{i})$			$(1, -2.7 - 0.4\text{i})$
e_{21}	$(1, -0.45 - 0.08\text{i})$		$(1, -3.2 + 0.6\text{i})$		

[1] E. Witten, A new look at the path integral of quantum mechanics, arXiv:1009.6032.

[2] E. Witten, Analytic continuation of Chern-Simons theory, arXiv:1001.2933.

[3] G. Basar, G. V. Dunne, and M. Unsal, Resurgence theory, ghost-instantons, and analytic continuation of path integrals, J. High Energy Phys. 10 (2013) 041.

[4] G. V. Dunne and M. Unsal, Deconstructing zero: Resurgence, supersymmetry and complex saddles, J. High Energy Phys. 12 (2016) 002.

[5] M. Cristoforetti, F. Di Renzo, A. Mukherjee, and L. Scorzato, Quantum field theories on the Lefschetz thimble, arXiv:1312.1052.

[6] E. Witten, A note on complex spacetime metrics, arXiv:2111.06514.

[7] F. Conrady and L. Freidel, On the semiclassical limit of 4-dimensional spin foam models, Phys. Rev. D **78**, 104023 (2008).

[8] J. W. Barrett, R. J. Dowdall, W. J. Fairbairn, F. Hellmann, and R. Pereira, Lorentzian spin foam amplitudes: Graphical calculus and asymptotics, Classical Quantum Gravity **27**, 165009 (2010).

[9] M. Han and M. Zhang, Asymptotics of spinfoam amplitude on simplicial manifold: Lorentzian theory, Classical Quantum Gravity **30**, 165012 (2013).

[10] E. Bianchi, E. Magliaro, and C. Perini, LQG propagator from the new spin foams, Nucl. Phys. **B822**, 245 (2009).

[11] M. Han, On spinfoam models in large spin regime, Classical Quantum Gravity **31**, 015004 (2014).

[12] M. Han, Z. Huang, H. Liu, and D. Qu, Complex critical points and curved geometries in four-dimensional Lorentzian spinfoam quantum gravity, Phys. Rev. D **106**, 044005 (2022).

[13] S. K. Asante, B. Dittrich, and H. M. Haggard, Effective Spin Foam Models for Four-Dimensional Quantum Gravity, Phys. Rev. Lett. **125**, 231301 (2020).

[14] M. Han and H. Liu, Analytic continuation of spinfoam models, Phys. Rev. D **105**, 024012 (2022).

[15] E. Bianchi, L. Modesto, C. Rovelli, and S. Speziale, Graviton propagator in loop quantum gravity, Classical Quantum Gravity **23**, 6989 (2006).

[16] E. Bianchi and Y. Ding, Lorentzian spinfoam propagator, Phys. Rev. D **86**, 104040 (2012).

[17] E. Magliaro and C. Perini, Emergence of gravity from spinfoams, Europhys. Lett. **95**, 30007 (2011).

[18] C. Perini, Einstein-Regge equations in spinfoams, J. Phys. Conf. Ser. **360**, 012050 (2012).

[19] E. Magliaro and C. Perini, Regge gravity from spinfoams, Int. J. Mod. Phys. D **22**, 1 (2013).

[20] M. Han, Semiclassical analysis of spinfoam model with a small Barbero-Immirzi parameter, Phys. Rev. D **88**, 044051 (2013).

[21] P. Dona, M. Han, and H. Liu, Spinfoams and high performance computing, arXiv:2212.14396.

[22] M. Han, Z. Huang, H. Liu, D. Qu, and Y. Wan, Spinfoam on Lefschetz thimble: Markov Chain Monte-Carlo computation of Lorentzian spinfoam propagator, Phys. Rev. D **103**, 084026 (2021).

[23] M. Han, Z. Huang, H. Liu, and D. Qu, Numerical computations of next-to-leading order corrections in spinfoam large-j asymptotics, Phys. Rev. D **102**, 124010 (2020).

[24] F. Gozzini, A high-performance code for EPRL spin foam amplitudes, Classical Quantum Gravity **38**, 225010 (2021).

[25] P. Frisoni, F. Gozzini, and F. Vidotto, Markov Chain Monte Carlo methods for graph refinement in spinfoam

cosmology, Classical Quantum Gravity **40**, 105001 (2023).
[26] P. Dona and P. Frisoni, How-to compute EPRL spin foam amplitudes, Universe **8**, 208 (2022).
[27] S. K. Asante, B. Dittrich, and J. Padua-Arguelles, Effective spin foam models for Lorentzian quantum gravity, Classical Quantum Gravity **38**, 195002 (2021).
[28] S. K. Asante, J. D. Simão, and S. Steinhaus, Spin-foams as semi-classical vertices: Gluing constraints and a hybrid algorithm, Phys. Rev. D **107**, 046002 (2023).
[29] S. K. Asante, B. Dittrich, and S. Steinhaus, Spin foams, refinement limit and renormalization, arXiv:2211.09578.
[30] B. Bahr and S. Steinhaus, Numerical Evidence for a Phase Transition in 4D Spin Foam Quantum Gravity, Phys. Rev. Lett. **117**, 141302 (2016).
[31] C. Rovelli and L. Smolin, Discreteness of area and volume in quantum gravity, Nucl. Phys. **B442**, 593 (1995).
[32] A. Ashtekar and J. Lewandowski, Quantum theory of geometry. 1: Area operators, Classical Quantum Gravity **14**, A55 (1997).
[33] M. Han and T. Krajewski, Path integral representation of Lorentzian spinfoam model, asymptotics, and simplicial geometries, Classical Quantum Gravity **31**, 015009 (2014).
[34] V. Bonzom, Spin foam models for quantum gravity from lattice path integrals, Phys. Rev. D **80**, 064028 (2009).
[35] J. Engle, W. Kaminski, and J. Oliveira, Addendum to 'EPRL/FK asymptotics and the flatness problem', Classical Quantum Gravity **38**, 119401 (2021).
[36] M. Han, Z. Huang, and A. Zipfel, Spin foam propagator: A new perspective to include the cosmological constant, Phys. Rev. D **97**, 084055 (2018).
[37] M. Han, Einstein equation from covariant loop quantum gravity in semiclassical continuum limit, Phys. Rev. D **96**, 024047 (2017).
[38] B. Dittrich and A. Kogios, From spin foams to area metric dynamics to gravitons, Classical Quantum Gravity **40**, 095011 (2023).
[39] J. W. Barrett, M. Rocek, and R. M. Williams, A note on area variables in Regge calculus, Classical Quantum Gravity **16**, 1373 (1999).
[40] A. Melin and J. Sjöstrand, Fourier integral operators with complex-valued phase functions, in *Fourier Integral Operators and Partial Differential Equations*, edited by J. Chazarain (Springer, Berlin, Heidelberg, 1975), pp. 120–223.
[41] L. Hormander, *The Analysis of Linear Partial Differential Operators I* (Springer-Verlag, Berlin, 1983), Chap. 7, Theorem 7.7.5.
[42] F. Conrady and L. Freidel, Path integral representation of spin foam models of 4d gravity, Classical Quantum Gravity **25**, 245010 (2008).
[43] J. W. Barrett, R. J. Dowdall, W. J. Fairbairn, H. Gomes, and F. Hellmann, Asymptotic analysis of the EPRL four-simplex amplitude, J. Math. Phys. (N.Y.) **50**, 112504 (2009).
[44] M.-X. Han and M. Zhang, Asymptotics of spinfoam amplitude on simplicial manifold: Euclidean theory, Classical Quantum Gravity **29**, 165004 (2012).
[45] P. Dona, M. Fanizza, G. Sarno, and S. Speziale, Numerical study of the Lorentzian Engle-Pereira-Rovelli-Livine spin foam amplitude, Phys. Rev. D **100**, 106003 (2019).
[46] M. Kapovich and J. J. Millson, The symplectic geometry of polygons in Euclidean space, J. Diff. Geom. **44**, 479 (1996).
[47] C. Rovelli and S. Speziale, A semiclassical tetrahedron, Classical Quantum Gravity **23**, 5861 (2006).
[48] L. Freidel and S. Speziale, Twisted geometries: A geometric parametrisation of SU(2) phase space, Phys. Rev. D **82**, 084040 (2010).
[49] P. Dona and S. Speziale, Asymptotics of lowest unitary SL(2, C) invariants on graphs, Phys. Rev. D **102**, 086016 (2020).
[50] S. K. Asante, B. Dittrich, and H. M. Haggard, Discrete gravity dynamics from effective spin foams, Classical Quantum Gravity **38**, 145023 (2021).
[51] H. Liu, https://github.com/LQG-Florida-Atlantic-University/extended_spinfoam (2021).
[52] D. Qu, https://github.com/dqu2017/4-simplex-amplitude-and-effective-dynamics-on-double-Delta3-complex (2021).
[53] S. Lefschetz, *The Picard-Lefschetz Theory* (Springer, New York, NY, 1975), pp. 135–148.
[54] A. Alexandru, G. Basar, P. F. Bedaque, and N. C. Warrington, Complex paths around the sign problem, Rev. Mod. Phys. **94**, 015006 (2022).
[55] M. Han, Semiclassical behavior of spinfoam amplitude with small spins and entanglement entropy, Phys. Rev. D **100**, 084049 (2019).
[56] M. Han, Z. Huang, and A. Zipfel, Emergent four-dimensional linearized gravity from a spin foam model, Phys. Rev. D **100**, 024060 (2019).
[57] A. Ashtekar, T. Pawlowski, and P. Singh, Quantum nature of the big bang: Improved dynamics, Phys. Rev. D **74**, 084003 (2006).
[58] A. Ashtekar, J. Olmedo, and P. Singh, Quantum Transfiguration of Kruskal Black Holes, Phys. Rev. Lett. **121**, 241301 (2018).
[59] D. Qu, https://github.com/dqu2017/Numerical-Asymtotics (2020).
[60] K. Tate and M. Visser, Realizability of the Lorentzian (n, 1)-simplex, J. High Energy Phys. 01 (2012) 028.
[61] K. Tate and M. Visser, Fixed-topology Lorentzian triangulations: Quantum Regge calculus in the Lorentzian domain, J. High Energy Phys. 11 (2011) 072.
[62] S. K. Asante, B. Dittrich, and J. Padua-Argüelles, Complex actions and causality violations: Applications to Lorentzian quantum cosmology, Classical Quantum Gravity **40**, 105005 (2023).
[63] B. Dittrich, S. Gielen, and S. Schander, Lorentzian quantum cosmology goes simplicial, Classical Quantum Gravity **39**, 035012 (2022).
[64] B. Dittrich, L. Freidel, and S. Speziale, Linearized dynamics from the 4-simplex Regge action, Phys. Rev. D **76**, 104020 (2007).